Aus dem Institut für Radiologie
der Medizinischen Fakultät Charité – Universitätsmedizin Berlin

DISSERTATION

Development and optimization of methods for quantitative Magnetic Resonance Imaging: QSM and DCE-MR

Entwicklung und Optimierung von Methoden zur quantitativen Magnetresonanztomographie: QSM und DCE-MR

zur Erlangung des akademischen Grades
Doctor of Philosophy (PhD)

vorgelegt der Medizinischen Fakultät
Charité – Universitätsmedizin Berlin

von

Matteo Ippoliti

aus Rom, Italien

Datum der Promotion: 17.09.2021

INDEX

List of Abbreviations

3D	Three-dimensional
AIF	Arterial Input Function
BW	Bandwidth
CNR	Contrast-to-noise-ratio
DCE-MR	Dynamic Contrast Enhanced Magnetic Resonance
DCE_f	Dynamic Contrast Enhanced late phase image
GRE	Gradient Recalled Echo
GRPE	Golden Radial Phase Encoding
ICC	Intra-class correlation coefficient
MC	Motion corrected
MEDI	Morphology Enabled Dipole Inversion
MNI	Montreal Neurological Institute
MR	Magnetic Resonance
NMC	Non motion corrected
PCA	Principal Component Analysis
QSM	Quantitative Susceptibility Mapping
RMSD	Root Mean Squared Displacement
ROI	Region Of Interest
SNR	Signal-to-noise-ratio
SPGR	Spoiled Gradient Echo
TA	Time of Acquisition
TE	Echo Time
TI	Inversion Time
TR	Repetition Time

ABSTRACT

(English)

Goal: Development and optimization of quantitative Magnetic Resonance Imaging (MRI) methods to provide enhanced image contrasts which can be used as potential biomarkers.

Methods: To achieve this goal, two studies were carried out: (i) optimization of Quantitative Susceptibility Mapping (QSM) in the brain. This study, based on 16 healthy volunteers, has consisted in evaluating reproducibility and consistency of QSM reconstructions obtained at 1.5T and 3T and in optimizing a sequence acquisition protocol to increase image contrast-to-noise ratio (CNR) at 1.5T. Four spoiled gradient echo (SPGR) acquisition sequences with different acquisition bandwidths were tested. (ii) implementation of a non-rigid respiratory motion correction (MC) framework for dynamic contrast enhanced MR (DCE-MR) imaging of the liver. DCE-MRI data was acquired at 3T during free breathing for 5 min, using a 3D T1-weighted Golden Angle Radial Phase Encoding (GRPE) sequence. Non-rigid respiratory motion information was extracted from the acquired data and used in a motion corrected image reconstruction to obtain high quality DCE-MRI images with temporal resolution of 6 s and isotropic resolution of 1.5 mm. An extended Tofts' model was fitted to the dynamic datasets, yielding quantitative parametric maps of endothelial permeability using the hepatic artery as input function. This new technique was evaluated on 11 oncological patients.

Results: As for the evaluation of reproducibility and consistency of QSM across field strenghts in (i), all four acquisition sequences reported very good correlation (Pearson correlation coefficient $R \geq 0.96$, widest limits of agreement I from -18.7 to 25.8 ppb). The CNR evaluation reported a statistically significant increase ($p < 0.05$) in four out of seven regions of interest (ROIs) for the lowest bandwidth employed with respect to the highest (25% increase in CNR of caudate nucleus). Motion correction in (ii), successfully removed respiratory motion artifacts and ensured accurate alignment between time points in the DCE-MR time-series, improving the average CNR of hepatic lesions in later phases of DCE-MR images by 47% ($p < 0.01$). CNR of endothelial permeability derived from motion corrected data was improved by 62% ($p < 0.01$) compared to images without motion correction. Motion correction also led to better identification and differentiation of pathologies such as hemangiomas, cysts and necrotic core tumors.

Conclusions: Both the optimized QSM acquisition protocol for 1.5T and the 3D non-rigid respiratory motion correction framework for DCE-MR images presented in this thesis improved the quality of quantitative MR images and led to a signfician increase of CNR over various features of interest.

(Deutsch)

Zielsetzung: Entwicklung und Optimierung von quantitativen Magnetresonanztomographie (MRI)-Methoden, zur Verbesserung von Bildkontrasten als neue Biomarker

Methoden: Um dieses Ziel zu erreichen, wurden zwei Studien durchgeführt: (i) Optimierung des Quantitative Susceptibility Mapping (QSM) im Gehirn. Diese Studie, die auf 16 gesunden Freiwilligen basiert, bestand in der Bewertung der Reproduzierbarkeit und Konsistenz der QSM Rekonstruktionen, die bei 1,5T und 3T erhalten wurden, sowie in der Optimierung eines Sequenzaufnahmeprotokolls zur Erhöhung des contrast-to-noise-ratio (CNR) bei 1,5T. Es wurden vier Spoiled-Gradient-Echo (SPGR) Aufnahmesequenzen mit unterschiedlichen Aufnahmebandbreiten getestet. (ii) Implementierung einer nicht-rigiden Methode zur Korrektur der Atembewegung (MC) für die Dynamic Contrast Enhanced MR (DCE-MR) Bildgebung der Leber. Die DCE-MR Daten wurden bei freier Atmung bei 3T für 5 Minuten unter Verwendung einer 3D T1-gewichteten Golden Angle Radial Phase Encoding (GRPE) Sequenz erfasst. Aus den erhaltenen Daten wurden Informationen über nicht-rigide Atembewegungen extrahiert und in einer bewegungskorrigierten Bildrekonstruktion verwendet um qualitativ hochwertige DCE-MRI Bilder mit einer zeitlichen Auflösung von 6 s und einer isotropen Auflösung von 1,5 mm zu erhalten. Ein erweitertes Tofts Modell wurde an die dynamischen Datensätze angepasst, wodurch sich quantitative parametrische Karten der endothelialen Permeabilität unter Verwendung der Leberarterie als Eingangsfunktion ergaben. Diese neue Technik wurde an 11 onkologischen Patienten evaluiert.

Resultate: Bezüglich der Bewertung der Reproduzierbarkeit und Konsistenz des QSM über Feldstärken in (i), wiesen alle vier Aufnahmesequenzen eine sehr gute Korrelation auf (Pearson-Korrelationskoeffizient $R \geq 0{,}96$, breiteste Grenzen der Übereinstimmung I von -18,7 bis 25,8 ppb). Die CNR-Auswertung wies einen statistisch signifikanten Anstieg ($p < 0{,}05$) in vier von sieben Regionen von Interesse (ROI) für die niedrigste verwendete Bandbreite im Vergleich zur höchsten (25% Anstieg des CNR des Nucleus Caudatus) auf. Die Bewegungskorrektur in (ii) minimierte erfolgreich Atembewegungsartefakte und gewährleistete eine genaue Ausrichtung zwischen den Zeitpunkten in der DCE-MR-Zeitreihe, wodurch sich die durchschnittliche CNR der Leberläsionen in späteren Phasen der DCE-MR-Bilder um 47% verbesserte ($p < 0{,}01$). Die CNR der endothelialen Permeabilität, die aus bewegungskorrigierten Daten abgeleitet wurde, verbesserte sich um 62% ($p <0{,}01$) im Vergleich zu Bildern ohne Bewegungskorrektur. Die

Bewegungskorrektur führte auch zu einer besseren Identifizierung und Differenzierung von Pathologien wie Hämangiomen, Zysten und nekrotischen Kerntumoren.

Schlussfolgerungen: Sowohl das optimierte QSM-Erfassungsprotokoll für 1,5T als auch die in dieser Arbeit vorgestellte 3D Methode zur nicht-rigiden Atembewegungskorrektur für DCE-MR Bilder verbesserte die Qualität der quantitativen MR Bilder und führte zu einem deutlichen Anstieg der CNR.

SYNOPSIS

Aim and Structure

Nowdays, medical imaging can be considered one of the cornerstones on which clinical interpretations and diagnoses are made. It is widely used in the clicical practice as qualitative assessment tool used to take clinical decisions. Quantitative Magnetic Resonance Imaging is a field involved with calculating biophysical parameters and quantities of interest, which have an effect on the MR signal that is encoded during the image formation process but at the same time are independent of hardware and acquisition protcol related parameters. In the specific case of MR, these quantities are related to a wide ensemble of physical and biophysical parameters. Physical parameters of interest include for example hydrogen spin density, relaxation times experienced by magnetization in soft tissue, diffusion and magnetic susceptibility to name a few, while biophysical parameters of interest include perfusion and blood flow velocities (1,2). The quantitative approach can in principle greatly aid in the correct diangnosis and interpretation of the image data, providing biophysical information that goes beyond what a purely visual assessment of the images might yield. In the latter case in fact, there is an intrinsic need for qualitative visual contrast between healthy and unhealthy tissue to be able to identify the differences. The estimation of quantitative parameters allows for a more precise interpretation of the imaged data, bypassing the need of a qualitative evaluation. It follows that this class of methods allows in principle for more sensible comparisons between different patients, scans and in the evaluation of treatment monitoring. The class of methods falling within this field therefore holds a great potential in terms of providing supplementary quantitative information to be exploited in the clinical setting in order for example to improve patient diagnosis, select and monitor the most appropriate therapies (2,3). On the other hand there are still many challenges revolving around this particular field and they are mostly related to the long acquisition times involved with the need of acquiring multiple qualitative scans to derive reliable quantitative information.

The goal of this thesis is to develop and optimize methods for quantitative Magnetic Resonance Imaging, with a particular focus on providing enhanced contrasts to be used as potential biomarkers. Two topics have been addressed in order to achive this goal: (i) the optimization of Quantitative Susceptibility Mapping (QSM) at the clinical field strength of 1.5T in order to increase contrast between features of interest in the brain. QSM is a viable novel contrast mechanism which is finding an evergrowing pool of applications, including tumor detection and study of neurodegenerative diseases; (ii) development of a three-dimensional (3D) non-rigid respiratory motion correction framework for dynamic contrast enhanced MR (DCE-MR) imaging in the liver during free-breathing. The latter can be used obtain functional parametric maps of hepatic metastases. The work reported in this synopsis has been published in two scientific articles in peer-reviewed journals. Specifically, QSM study has been published in (4) and motion correction of DCE-MR in (5).

The synopsis is structured as follows: section 1 is an introduction, in which the current research scenario about QSM and respiratory motion correction is outlined, while details about the methods employed and the main results are given in section 2 and section 3, respectively. Section 4 presents a discussion about the improvements produced by this work and future outlook. In section 5 the main conclusions of this work are summarized.

1 - INTRODUCTION

1.1 QSM

Scientific Context

Quantitative susceptibility mapping (QSM) is a newly introduced post-processing method in magnetic resonance (MR) imaging, employed to compute maps of apparent magnetic susceptibility of the underlying examined tissue (6). Magnetic susceptibility is a physical property that characterizes the response of an object when placed inside an external magnetic field (7). On the one hand, strong susceptibility variations within an object, for example at the air-tissue interfaces in the human brain, generate field distortions both locally and at longer ranges that can be propagated in the final MR images as geometric distortion artefacts (8, 9). On the other hand the small field distortions created by the variations in susceptibility within soft tissues, are sufficiently small to be exploited as MR image contrast (7). QSM maps can provide for the first time, quantitative information on the spatial distribution of magnetic susceptibility sources such as calcium, iron, gadolinium, blood products and super paramagnetic iron oxide nano particles and therefore hold great potential as clinical biomarkers (10). The main idea behind this technique is to solve the magnetic-field-to-susceptibility-source inverse problem, by performing a dipole deconvolution, which is challenged by the lack of MR signal in areas where susceptibility sources are present and by the zeroes that arise in the dipole kernel, making the problem ill-posed and therefore giving rise to several solutions (11).

Different approaches exist in the current literature to obtain QSM maps. These include different types of acquisition sequences to acquire raw data (i.e. magnitude and phase) and also different reconstruction algorithms used in post-processing. Regarding the acquisition, Gradient Echo (GRE) sequences are considered most appropriate as they generate phase maps that contain information on the fluctuations experienced by the magnetic field due to the underlying susceptibility distribution (12). Although a single-echo GRE acquisition (13), is in principle sufficient to reconstruct QSM, in recent years the use of multiple echoes has found broader consensus due to the inherent capability of probing a wider range of tissues susceptibilities (6, 14) and with increased signal-to-noise-ratio (SNR) with respect to single-echo imaging (15, 16). Different acquisition strategies have been tested through variation of the MR sequence readout, employing for example spiral imaging (15), 2- and 3-dimensional echo planar imaging (EPI) (13, 17). The QSM reconstruction per se, is a complex procedure which involves several steps, such as phase unwrapping, background field removal and finally field to susceptibility inversion. A comprehensive description of the above mentioned steps and of the currently developed algorithms apt at solving them based on different strategies, can be found for example in (6). More specifically, some algorithms have implemented the use of regularization to compute QSM (18, 19, 14). One such algorithm is the Morphology Enabled Dipole Inversion (MEDI) algorithm (19, 20), which utilizes tissue morphological information derived from magnitude images, acquired through 3D multi-echo spoiled gradient echo (SPGR) sequences and the magnetic susceptibility maps, to apply Bayesian regularization and solve the inverse problem robustly.

Several applications have been developed based on the use of QSM including: investigation of iron accumulation in deep gray matter structures which is associated with Parkinson’s disease, quantification of gadolinium in contrast-enhanced MR and the evaluation of micro bleeds, hemorrhages, calcifications in the brain and the detection of some tumors (4). More recent QSM applications have focused on improving anatomical depiction in deep gray matter structures together with improving quantitative measurements of functional imaging parameters such as perfusion and oxygenation, which in turn could be used for the assessment of strokes and tumors (21, 22).

Motivation and Challenges

One of the main challenges faced today in the clinical implementation of QSM rests in the variability of reproducibility and consistency of QSM reconstructions, which renders multi-center and comparative studies hard to achieve (23, 24). This variability can be attributed to different factors, spanning from acquisition protocols to QSM reconstruction algorithms to the clinical field strengths employed (1.5T and 3T), which render multi-center and comparative studies hard to achieve (23, 25). Therefore, the challenges undertaken by this work were to firstly evaluate the reproducibility and consistency of QSM values obtained through a specific algorithm and SPGR acquisition protocol, on two different field strengths of 1.5T and 3T of a single vendor. Secondly, even if 3T scanners can generally achieve higher image quality thanks to the two-fold increase in SNR with respect to the 1.5T counterparts (25), the lower field alternative is still most commonly found in the clinical setting (26, 27). It is was therefore deemed worth investigating whether the image quality of QSM reconstructions obtained at 1.5T may be enhanced through the acquisition protocol. Specifically, the variation of the acquisition bandwidth was evaluated for this purpose, because of the direct effect it exerts on the sampling and echo times which in turn have an influence on the sampled noise and magnitude of the susceptibility artifact in GRE images (28). In order to quantify the effect on the final QSM maps of this parameter alone, a specific set of SPGR protocols was designed, in which only bandwidth and strictly related acquisition times were varied, while all other factors were kept constant. This implied testing on a group of healthy volunteers, acquired on the same 1.5T machine and processed with the same algorithm to yield QSM maps. The choice of the MEDI algorithm seemed most appropriate for this study, thanks to the recently introduced L1 regularization (19,20), which potentially introduces a more robust framework for resolving QSM especially in diseased subjects with areas of lower SNR in the brain (24).The aim of this work (4) was to evaluate the reproducibility and consistency of QSM reconstructions obtained with the MEDI algorithm on two different field strengths of 1.5T and 3T, followed by the evaluation of image quality enhancement in terms of contrast-to-noise-ratio (CNR) obtainable on 1.5T through variation of the acquisition bandwidth.

1.2 Motion Correction

Scientific Context

Dynamic Contrast-Enhanced Magnetic Resonance Imaging (DCE-MR) is a powerful qualitative and quantitative tool, used in oncological examinations of the liver to identify metastases in T1-weighted anatomical MR scans (29-31). The technique is based on the study of the uptake dynamics (contrast uptake curve) in the tissue of interest, of a paramagnetic MR contrast agent that is injected intravenously during the examination. Using qualitative images, it is capable of easily contrasting healthy tissue from metastatic tissue in the late phases of the contrast uptake curve. Using quantitative pharmacokinetic modeling, it can be used to derive important functional information from the anatomical DCE-MR time-series. This yields a series of complimentary functional parametric maps, such as: the endothelial permeability (K_{trans}), the fractional volume of contrast agent present in the vascular compartment (v_p) and the fractional volume of contrast agent contained in the extravascular extracellular compartment (v_e) (31). However, it is often not possible in the clinical setting to derive such maps from the DCE-MR time-series of the liver, as the number of image volumes acquired in time is rather limited (3 to 5 phases), due to restrictions imposed by respiratory motion. A reliable fit of the pharmacokinetic model using only so few phases is often not possible. Respiratory motion is a major challenge in DCE-MR of the liver, where it leads to motion artifacts, image blurring and misregistration between neighboring temporal phases. These artifacts are propagated through the pharmacokinetic model into the final maps. To minimize respiratory motion during examinations, the clinical standard requires patients to hold their breath up to 15 seconds at different phases of the contrast uptake curve (33). This practice has shown to yield anatomical T1-weighted images with good image quality and high in-plane spatial resolution, but often suffers from: incompliance from patients with impaired breathing, low slice resolution and misregistration between the different dynamic phases, as no two breath-holds can be easily repeated identically and the organs' position differs each time. Regarding this last case, some studies have attempted to minimize misalignment of the organs through registration in post-processing (34, 35). Furthermore, as introduced in the previous paragraph, breath-holding only allows for the acquisition of a few DCE phases, strongly limiting the applicability of a pharmacokinetic model. Other common approaches utilized to minimize the negative effects introduced by respiratory motion, involve the use of free-breathing and fast acquisition techniques such as radial imaging, parallel imaging and compressed sensing (36-38). These approaches however are limited in terms of achieved signal-to-noise-ratio (SNR) and low through-plane resolution, in addition to being affected by residual motion artifacts. Lastly, a number of studies have also attempted to resolve the motion issue by registering the DCE phases to a reference both rigidly (39) and non-rigidly (40,41), but they have only been demonstrated to work for a limited number of time points (3 to 4) and/or with an intermediate slice resolution. Furthermore, methods that involve registration may not be very well suited for DCE, if they do not take into consideration the signal variations that are induced by the presence of the MR contrast agent other than respiration alone. This effect would in fact then result in a bias in the measured image intensity that can be erroneously processed by the registration algorithms (42).

Motivation and Challenges

Respiratory motion is an important obstacle in the correct derivation of DCE-MR dynamic datasets, as it hampers both the qualitative and quantitative nature of the images. Current clinical and experimental DCE-MR protocols often lack the required spatial and temporal resolutions required to fully exploit the pharmacokinetic modeling and the characterization of small features of interest. Sources of variability (43), together with that induced by respiratory motion, pose a practical limitation to the standardization needed to make quantification comparisons across studies that are carried out with different acquisition strategies or post-processing and data analysis techniques (44, 45). The aim of this work (5) was therefore to develop a novel approach to acquire DCE images of the abdomen with high spatial (1.5 mm isotropic) and high temporal (6 s) resolution during free breathing, that would allow for enhanced visualization and quantitative characterization of small hepatic lesions. Non-rigid motion correction was used to minimize respiratory motion artifacts and to ensure accurate functional maps can be derived from the qualitative DCE images using an Extended Tofts Pharmacokinetic Model (32). A data analysis framework was therefore also developed on top of the motion correction, to carry out the pharmacokinetic modeling. Data was acquired using a 3D Golden Angle Radial Phase Encoding (GRPE) protocol, which is particularly suited for undersampling and for extracting a robust respiratory navigator from central k-space lines, which are periodically acquired (46). In this manner, all necessary information for the motion correction (i.e. self-navigator signal, coil sensitivity information and motion displacement fields) are derived from the DCE data. There was therefore no need for external motion tracking devices or any additional MR scans and 100% scan efficiency was ensured.

2 - METHODS

2.1 QSM

Study Population and Data Acquisition

The study was conducted on a population consisting of 16 healthy volunteers (6 women; mean age 27.8 ± 3.2 years) with no history of any relevant disease who provided written informed consent and was approved by the local review board. Two MR scanners (Siemens Healthcare, Erlangen, Germany), a Siemens Magnetom Avanto of 1.5T and a Siemens Magnetom Skyra of 3T, were used in the experiment to scan each subject once with each field strength and with identical scan sessions. A scan session consisted in four variations of an SPGR protocol that were named QSM-1 to QSM-4 and were used in the subsequent QSM reconstructions, together with a 3D anatomical T1-weigthted scan consisting of a magnetization-prepared rapid gradient-echo (MPRAGE). The MPRAGE images were necessary in order to carry out the segmentation of the brain and normalization to the Montreal Neurological Institute (MNI) space of QSM images. The experiment was designed this way in order to evaluate the reproducibility and consistency of the QSM reconstructions across the two employed field strengths and across four distinct receiver bandwidths. The latter evaluation will also serve in a quantitative assessment of image quality for the 1.5T QSM images. The SPGR protocols share the following common acquisition parameters: field of view = 240 mm; matrix size = 260 × 320 × 60; slice thickness = 3 mm; flip angle = 15°; parallel imaging factor = 2. Each of the four SPGR protocols differs from the others in: initial echo time (TE_0); temporal spacing between each echo (δTE); number of echoes (n); receiver bandwidth (BW); acquisition time (TA). Characteristic parameters for the individual protocols are reported in Table 1. The MPRAGE protocol was acquired on both scanners with the following parameters: field of view = 230 mm, matrix size = 256 × 256 × 176; slice thickness = 1 mm; flip angle = 8°; inversion time (TI) = 900 ms; echo time (TE) = 2.5 ms; repetition time (TR) = 2200 ms; parallel imaging factor = 2.

SPGR Characteristic Sequence Parameters

SPGR	TE_0 [ms]	δTE [ms]	n	BW [Hz/Px]	TA [min]
QSM-1	6.4	4.1	10	260	4:32
QSM-2	7.1	5.3	8	200	4:32
QSM-3	7.5	5.8	8	180	4:54
QSM-4	8.1	6.9	8	150	5:44

Table 1: SPGR sequence-specific custom parameters. The presented table is based on previously published work in (4).

Image Processing and Statistical Analysis

QSM maps of each subject were obtained through the software MEDI (19, 20) and setting the regularization parameter to 1000 for all subjects. In essence the algorithm first generates a magnitude image and an unwrapped phase image from the SPGR data. Secondly the background field is removed and a map of the field represented by the tissue alone is created. Lastly the QSM maps are obtained from the joint use of the magnitude images with the tissue field maps in the dipole inversion process (11).

In order to evaluate the reproducibility and consistency of QSM maps obtained at different field strengths at a group level, these needed first to be coregistered for each subject to the MPRAGE of the respective field strength and normalized to MNI space. An average QSM template was then generated in this space for each subject to draw masks of regions of interest (ROI) around several structures in the brain (set I). As a last step, these masks were used to carry out an ROI-based evaluation through Bland-Altman analysis (difference (M) and limits of agreement (I)) and linear regression analysis (Pearson correlation coefficient (R) and slope of regression line (b)) on the normalized QSM maps of each subject. Moreover, a voxelwise-based evaluation on whole-brain normalized QSM maps, obtained through averaging over subjects for each BW, was also carried out.

The CNR evaluations were designed to quantitatively investigate the variations in image quality while varying the acquisition bandwidth. QSM-1 to QSM-4 maps were coregistered to the average magnitude image obtained for each subject, and were then also averaged to create a template apt at drawing a new set of ROIs (set II) identified by the caudate nucleus, globus pallidus, red nucleus, putamen, splenium, thalamus and substantia nigra. The CNR was then calculated for each ROI in set II on the QSM map of all subjects, according to the following:

$$CNR = \frac{\bar{S}_I - \bar{S}_O}{\sigma_O} \tag{1}$$

where $\bar{S}_I$ represents the mean QSM value measured inside each ROI, $\bar{S}_O$ is the mean QSM value measured in an external ROI encircling but not comprising $\bar{S}_I$ and σ_O is the standard deviation of the external ROI. Weighted average and respective standard deviations ($\overline{CNR} \pm \sigma_{\overline{CNR}}$) were calculated over all subjects, using the number of voxels from each ROI as weights. Percentage variations of $\overline{CNR}$ values were also calculated across maximum and minimum BW for each ROI. The unequal-variances t-test was used to verify the statistical significance of the $\overline{CNR}$ differences, set at $p < 0.05$.

All the image processing and statistical analyses were implemented in an automated custom Matlab pipeline (2016b, The Mathworks, Natick, MA) making use of SPM12 (Wellcome Department of Imaging Neuroscience, University College London, United Kingdom) (47). Masks were manually drawn with FSLView (48).

Image Quality Assessment

A qualitative image analysis was performed by two radiologists (one with board certification), that consisted in visually evaluating and comparing the image quality of QSM maps, specifically set II of ROIs, over varying BW with a five-point linear grading scale (from 1 = non-diagnostic to 5 = excellent quality). Inter-observer reliability was established through the intra-class correlation coefficient (ICC), varying from poor (ICC < 0.4) to excellent (ICC > 0.75). Statistical significance in the differences in image quality evaluation were assessed through the Wilcoxon rank sum test, with $p < 0.05$.

2.2 Motion Correction

Study Population and Data Acquisition

This study involved the enrollment of 11 patients from oncology, who were being examined through whole-body hybrid Positron Emission Tomography and Magnetic Resonance (PET-MR) Imaging on a 3T Biograph mMR (Siemens Healthcare, Erlangen, Germany) to investigate the presence of established and/or presumed hepatic metastases (5 patients) or to investigate other pathologies unrelated to hepatic imaging (6 patients). The former group received an injection of 0.01 mmol/kg of Gadoxeate disodium (relaxivity (r) at 3T of 6.2 mM^{-1} s^{-1}) as the MR contrast agent, while the latter received an injection of 0.1 mmol/kg of Gadobutrol (r at 3T of 5 mM^{-1} s^{-1}). All injections took place approximately 1 min after the start of the scan. The study was approved by the local review board and written informed consent was provided by all patients. A total of 19 lesions could be identified across all patients and were used for quantitative evaluations of the proposed motion correction approach.

The DCE-MR scan protocol employed in this experiment consisted of a 3D Gradient Recalled Echo (GRE) T1-weighted GRPE scheme with fat suppression (49), which is characterized by radial sampling in the phase encoding plane and by a Cartesian readout along the foot-heat direction. Relevant imaging parameters for this protocol are: field of view = 288 × (288 – 345) × (288 – 345) mm^3; matrix size = 192 × 120 × 640; resolution = 1.5 × 1.5 × 1.5 mm^3; Partial Fourier Factor = 5/8; TE = 1.36 ms; TR = 3.3 ms; flip angle = 12°; TA = 4 min. A

Turbo Spin Echo with fat suppression was also acquired to characterize metastases as part of the standard clinical protocol.

Derivation of Respiratory Self-Navigator and Respiratory Motion Estimation

In a first step a self-navigator is obtained from the k-space center lines sampled along the foot-head direction (50) describing the internal abdominal motion. Nevertheless, it is also influenced by the MR contrast agent uptake dynamic. Therefore, a principal component analysis (PCA) is applied in order to select the component with the most prominent signal variations induced by respiration. This step is achieved by evaluating the frequency spectrum of each PCA component and selecting the one with the highest energy in the typical frequency domain of respiration (0.1−0.5 Hz). Lastly, PCA is applied to the concatenation of the all the identified respiratory components from all coils to yield a single respiratory self-navigator. The acquired MR raw data is then separated into eight different respiratory motion states (MS) based on the amplitude of the self-navigator signal.

Motion information in the form of vector motion fields (MF) is then obtained through registering non-rigidly (51), the various MS to a reference. Prior to carrying out this step, it is necessary to reconstruct the k-space MS to image space and this is achieved iteratively with a sensitivity-encoding method (52):

$$\hat{x} = min\left(\|Ex - k\|_2^2 \;+\; \lambda_t \mathrm{TV}_t \;+\; \lambda_s \mathrm{TV}_s\right) \tag{2}$$

with $\hat{x}$ being the reconstructed image of a specific MS; E being the encoding operator; k representing the k-space data in the selected MS; TV_t and TV_s representing the total image variation in time measured in temporally adjacent MS and the total image variation in space inside the selected MS, respectively; λ_t and λ_s represent the regularization parameters employed to adjust the regularization process which were selected constant for all patients.

Implementing Motion Correction

Once the MFs have been calculated for each MS, motion correction of the DCE-MR time series can be applied inside an iterative kt-SENSE image reconstruction framework (53) to yield 48 dynamic phases with a temporal resolution of 6 s. The k-space data employed to generate each DCE-MR phase is selected with a sliding-window approach. With the aid of the respiratory navigator each phase is divided into 8 MS, which are then reconstructed to image space where they are shifted to the reference MS through the MFs. The kt-SENSE image reconstruction framework can be described by the following:

$$\hat{x} = min\left(\left\|E\mathcal{F}_{f\to t}x - k\right\|_2^2 + \lambda\|P^{-1}x\|_2^2\right) \tag{3}$$

where $\hat{x}$ is the entire DCE-MR image time series (48 phases) given in the temporal frequency domain; E is the encoding operator and contains the MF necessary to implement motion correction; $\mathcal{F}_{f\to t}$ is the Fourier transform from frequency to time domain; k is the k-space data; λ is the regularization parameter; P represents a training dataset of low spatial resolution DCE-MR images used to aid in separating the effects on the DCE images of the undersampling artifacts from the ones of the MR contrast uptake, selectively suppressing the former in the regularization process. All image the image reconstructions (respiratory motion estimation and motion-corrected DCE-MR image reconstruction) were implemented in Python (Python Software Foundation) and Matlab (R2016b, The Mathworks, Natick, MA). In addition to the motion-corrected (MC) data sets also non-motion corrected images were reconstructed (NMC) for reference.

Functional Parametric DCE Maps and Quantitative Motion Correction Analyses

In order to perform quantitative investigations on the DCE datasets, it is first necessary to convert the image intensities from arbitrary units to the concentration of contrast agent expressed in mM. This step is achieved by implementing a single-reference tissue method for heavily T1-weighted acquisition protocols in a custom pipeline (54, 55):

$$c(t) \cong \frac{(I(t) - I_0)}{r\, T_1^{ref} I_0^{ref}} \tag{4}$$

where $I(t)$ is the image intensity in a given voxel in the liver at time t; I_0 and I_0^{ref} represent the image intensity measured before the injection of the MR contrast agent in a given voxel in the liver and in reference tissue (liver parenchyma) respectively; $c(t)$ is the concentration of contrast agent in mM at time t; T_1^{ref} is the T1 value of the reference tissue before contrast injection (56) and r is the relaxivity of the contrast agent (57). Once the DCE-MR timeseries are converted, the Extended Tofts' Model (32) can be resolved, extrapolating functional parametric maps of the liver, according to the following:

$$c(t) = v_p AIF(t) + K_{trans} \cdot e^{-\frac{K_{trans}}{v_e} \cdot t} * AIF(t - t') \tag{5}$$

where K_{trans} is the volume transfer constant characterizing the flow of contrast agent from the vascular compartment to the tissue compartment, therefore representing permeability and is expressed in min^{-1}; c(t) is once again the contrast agent uptake in a given voxel of interest and expressed in mM; v_p is the fractional volume of contrast agent contained in bold plasma; v_e is likewise the fractional volume of contrast agent contained in the extracellular space; t' is the time delay in min between the MR contrast injection and the peak of enhancement registered in the tissue of interest; $*$ represents the convolution operator and the AIF is known as the Arterial Input Function and represents the contrast agent concentration measured in mM in the vascular compartment. We attempted to sample the AIF in both the aorta and the smaller hepatic artery, in order to show the bias respiratory motion can induce on the shape of the AIF of smaller vascular structures.

The maximum displacement of all lesions due to respiratory motion was measured based on the motion fields. This was done by first manually masking in FSLView (48), the hepatic metastases in the latest phase of the DCE-MR image series (DCE_f) where they appear most evidently, and subsequently calculating the root mean squared displacement (RMSD) experienced in average by each mask. The second part of the evaluation was designed to specifically verify the effects of the proposed motion correction method on the image contrast over the lesions. Particular attention was given to small structures which tend to be heavily blurred or disappear in DCE-MR images that are not corrected for respiratory motion. The evaluation involves measuring the CNR of each lesion, with the aid of the same masks introduced in the previous paragraph, with respect to the healthy tissue surrounding the lesion. Equation 1 is used to calculate the CNR over the lesions from DCE_f and also from the functional K_{trans} maps. The average CNR and relative standard deviation are calculated for MC ($\overline{CNR}_{MC} \pm \sigma_{MC}$) and NMC ($\overline{CNR}_{NMC} \pm \sigma_{NMC}$) datasets respectively. The normality assumption of the $\overline{CNR}$ distributions was first verified by a Kolmogorov-Smirnov test, while the statistical significance in the difference of values was assessed with an equal-variances t-test. The p value was set to be < 0.05 for both tests.

3 - RESULTS

3.1 QSM

Statistical Analysis

The reproducibility and consistency assessment of all employed SPGR protocols and respective QSM map, obtained on the two different field strengths and for equal protocols, in both the whole-brain voxelwise-based analysis and ROI-based analysis for set of ROIs I, are reported in Table 2. As a general trend it can be observed that all four the SPGR sequence variations produced QSM maps with very high inter-field correlation ($R \geq 0.9$, $|M| \leq 0.14$, $-9.28 \leq I \leq 9.09$) already at the voxelwise-based level and even higher at a ROI-based level ($R \geq 0.96$, $|M| \leq 3.6$, $-18.7 \leq I \leq 25.8$), with a slight decrease along with decreasing BW, going from QSM-1 to QSM-4. As for the reproducibility investigations conducted specifically over different BW (QSM-1 vs QSM-4) and acquired at equal field strengths (Table 2), it can also be appreciated that the level of correlation is very high between the tested sequences both at the voxelwise level ($R \geq 0.93$, $|M| \leq 0.03$, $-7.69 \leq I \leq 7.63$) and at ROI level ($R \geq 0.99$, $|M| \leq 0.4$, $-16.1 \leq I \leq 15.6$).

Table 2 - Statistical results of reproducibility of QSM across field strengths and BW

	Sequences	***R***	***b***	***M* [ppb]**	***I* [ppb]**
Voxelwise-based	QSM-1	0.93	1.02	0.06	-7.14 to 7.02
	QSM-2	0.92	1.02	0.14	-8.27 to 7.99
	QSM-3	0.91	1.03	0.05	-8.62 to 8.54
	QSM-4	0.90	1.03	0.09	-9.28 to 9.09
ROI-based	QSM-1	0.98	1.09	2.9	-15.7 to 21.4
	QSM-2	0.98	1.06	2.7	-15.7 to 21.2
	QSM-3	0.97	1.06	3.6	-18.7 to 25.8
	QSM-4	0.96	1.03	2.1	-17.3 to 21.5
Voxelwise-based	QSM-1 vs QSM-4 (1.5T)	0.97	1.02	0.01	-4.24 to 4.26
	QSM-1 vs QSM-4 (3T)	0.93	1.03	-0.03	-7.69 to 7.63
ROI-based	QSM-1 vs QSM-4 (1.5T)	0.99	1.00	0.4	-16.1 to 15.6
	QSM-1 vs QSM-4 (3T)	0.99	0.96	-0.3	-12.7 to 12.1

Results of voxelwise and ROI-based QSM reproducibility and consistency analyses over different field strengths and fixed BW and over fixed field strengths and varying BW. M is the mean difference, I are the limits of agreement set at 95%, R is the Pearson correlation coefficient and b is the slope of the regression line. The presented table is based on previously published work in (4).

The quantitative CNR (set of ROIs II) evaluation carried out between QSM-1 and QSM-4 at 1.5T and apt at verifying the possibility of increasing image contrast over brain structures at this specific field strength by optimizing the acquisition BW, has shown a statistically significant increase in the $\overline{CNR}$ values of 4 out of 7 regions. The interested ROIs and respective CNR percentage increase are: caudate nucleus (25%); thalamus (19%), red nucleus (15%) and substantia nigra (13%). The putamen, globus pallidus and splenium also registered an increase in the average CNR (13%, 8% and 6% respectively), but were not found to be statistically significant according to the sample size. An overview of the differences in image quality and contrast obtained at 1.5T for QSM-1 and QSM-4 is displayed in Figure 1, where the caudate nucleus, globus pallidus and putamen are also put in evidence.

The qualitative analysis of QSM images obtained at 1.5T and carried out by two independent radiologists on set of ROIs II, has also reported results with good inter-observer agreement (ICC median = 0.65 and interquartile range from 0.49 to 0.82), but also in good agreement with the CNR findings discussed in the last paragraph. In essence, significant increase in QSM image quality were found in all ROIs except the splenium when comparing QSM-1 to QSM-4, with an average percentage increase in the observer scores for the thalamus (40%), substantia nigra (39%), red nucleus (34%), putamen (32%), caudate nucleus (20%) and globus pallidus (17%).

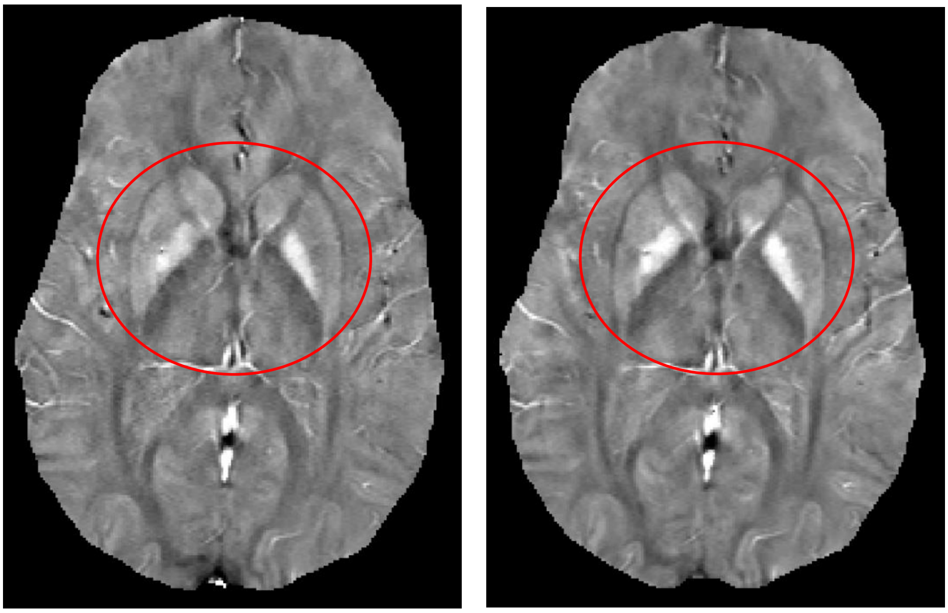

Figure 1: Axial slice of QSM maps reconstructed from QSM-4 (left) and QSM-1 (right), acquired at the field strength of 1.5T. The red circle highlights the caudate nucleus, globus pallidus and putamen. The presented figure has been adapted from previously published work in (4).

3.2 Motion Correction

Motion Correction Assessment on Hepatic Lesions

The evaluation of lesion displacement through the use of the RMSD, resulted to be in average 3.82 ± 1.11 mm along the main direction of motion (ie. foot-head direction) and with a maximum recorded displacement of 5.19 mm for individual lesions. Figure 2a depicts the blurring effects induced by respiratory motion on a hepatic lesion (red circle) and shows the improvements in image quality and contrast achieved by motion correction. In the MC dataset, the edges of the liver and surrounding structures are well defined and sharp. The lesion can be identified well in the later phases of the MC dataset, which does not hold true for the NMC.

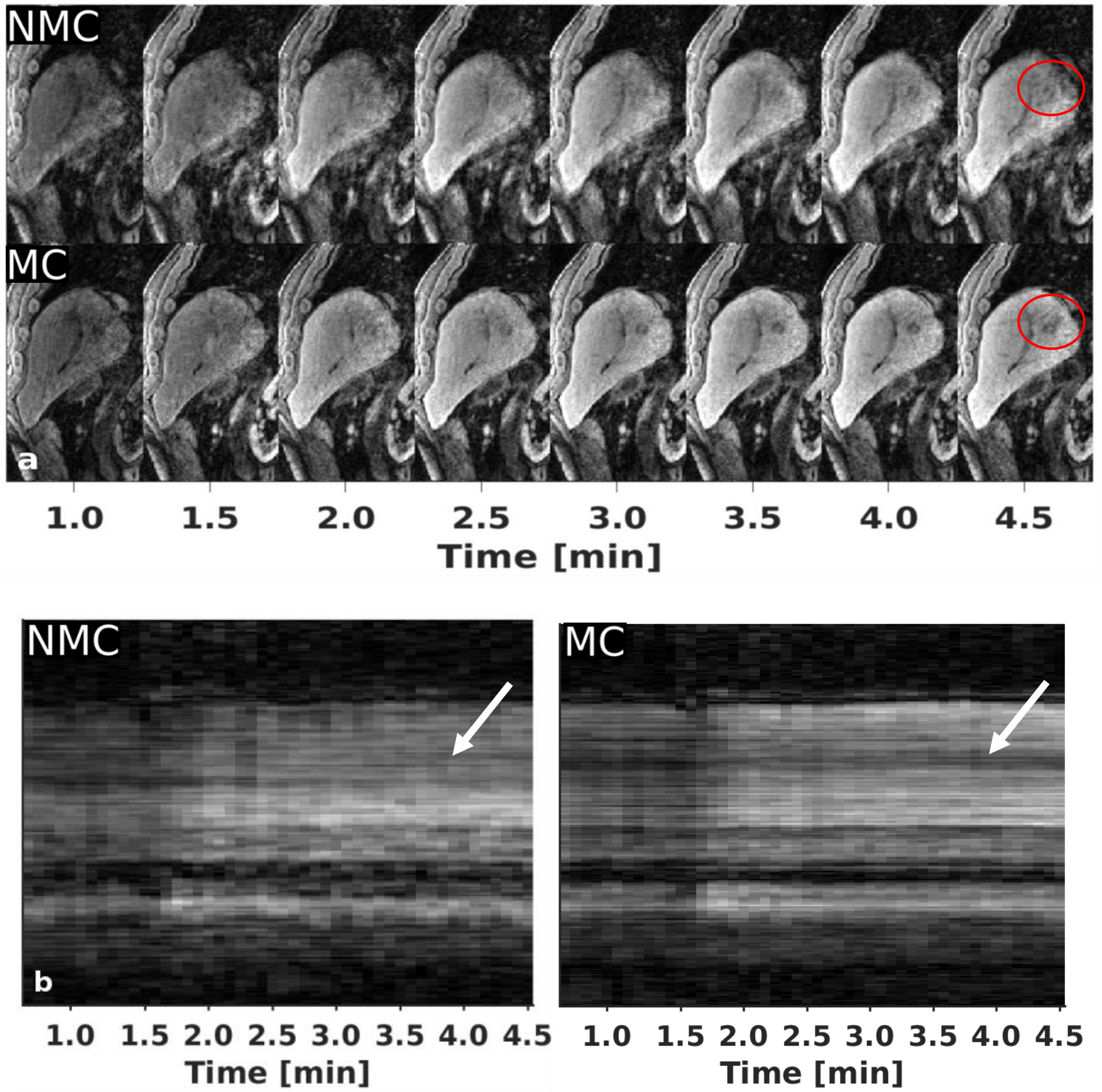

Figure 2: (a) DCE-MR sagittal section of a patient through the center of a hepatic lesion (red circle) and depicting contrast uptake throughout the whole sequence acquisition. (b) Time evolution of a line of

voxels going through the center of the lesion along the foot-head direction. The presented figure was based on data published in (5).

Figure 2b shows the temporal evolution of a line of voxels drawn along the foot-head direction and passing through the center of the lesion depicted in Figure 2a. As can be seen in the section where the lesion is present (white arrow), the MC dataset shows a dark segment which highlights the typical uptake behavior of a lesion, while in the NMC dataset the induced blurring noticeably reduces the contrast on the tumor to the surrounding healthy liver tissue. The CNR analysis of the 19 lesions conducted on the MC and NMC DCE$_f$ images showed significant average percentage increase of 47% in favor of motion correction, confirming the qualitative findings.

Sampling of the AIF in the aorta resulted to be almost identical for MC and NMC curves of most patients, while in the hepatic artery the uptake curves differed particularly in the shape of the peak, which appeared suppressed with respect to MC as can be seen in Figure 3. The MC contrast uptake curve of the lesion (blue curve) showed the typical early rise in signal followed by a quick descent found in malignancies, while the NMC curve showed a delayed rise followed by a plateau (red curve), as did the healthy tissue (green curve).

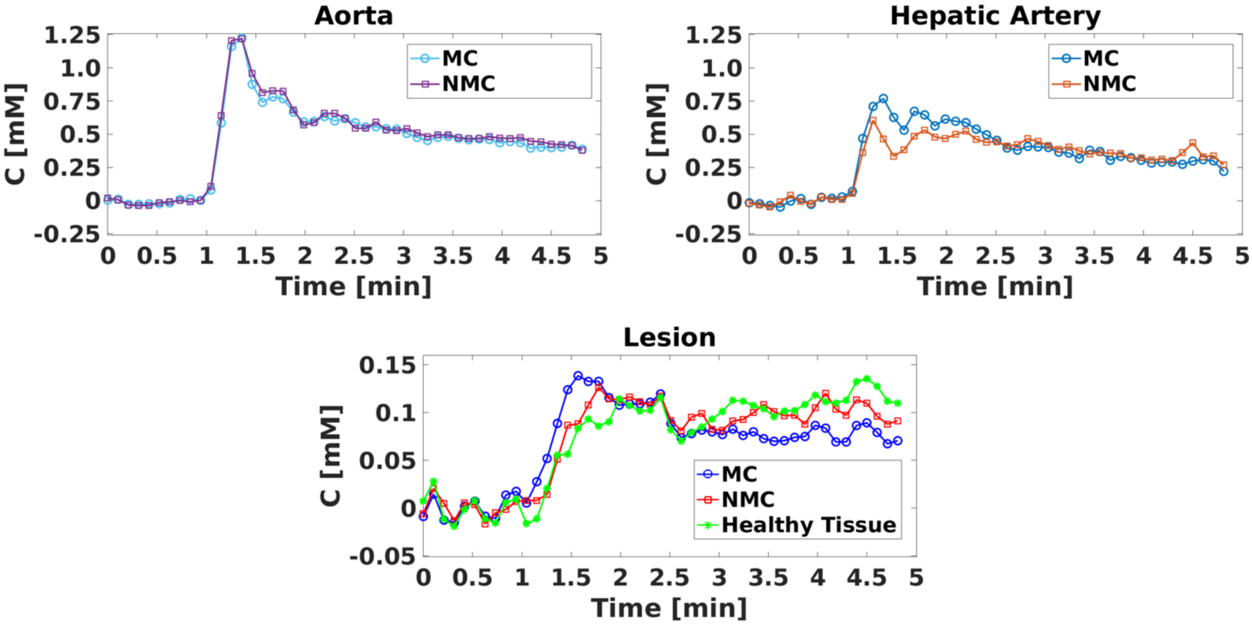

Figure 3: AIF sampling in the Aorta, Hepatic Artery for MC and NMC data. Sampling of contras uptake curve in a lesion for MC and NMC data and in healthy tissue for MC data only. The presented figure was based on data published in (5).

Figure 4 shows the MC and NMC coronal section of the liver cutting through a number of lesions (black circles) in the DCE$_f$ (Figure 4a and Figure 4b) images and K_{trans} maps (Figure 4d and Figure 4e). Some metastases (black ellipse) do not appear clearly in either MC or NMC DCE$_f$ images but can be distinguished in K_{trans} maps and their presence is further confirmed by inspecting the Turbo Spin Echo image (Figure 4c). In the MC K_{trans} map as well as in the MC DCE$_f$ image, it is possible to distinguish some metastases that are severely blurred in the NMC (three smaller black circles). Especially in the K_{trans} map the smaller focal lesions are well distinguished with respect to their background in MC while tend to either completely vanish or blur into their surroundings. Furthermore, the level of noise in terms of blurring is noticeably higher in both NMC images. The results of the CNR evaluation averaged over 10 lesions demonstrated a statistically significant percentage increase of $\overline{\mathrm{CNR}}_{\mathrm{MC}}$ = 62% for MC. The motion correction framework improved the detection of other features such as cysts, hemangiomas and tumors with necrotic substructures, as can be seen in an example shown in Figure 5, where the central region of the lesion is characterized by very low permeability values.

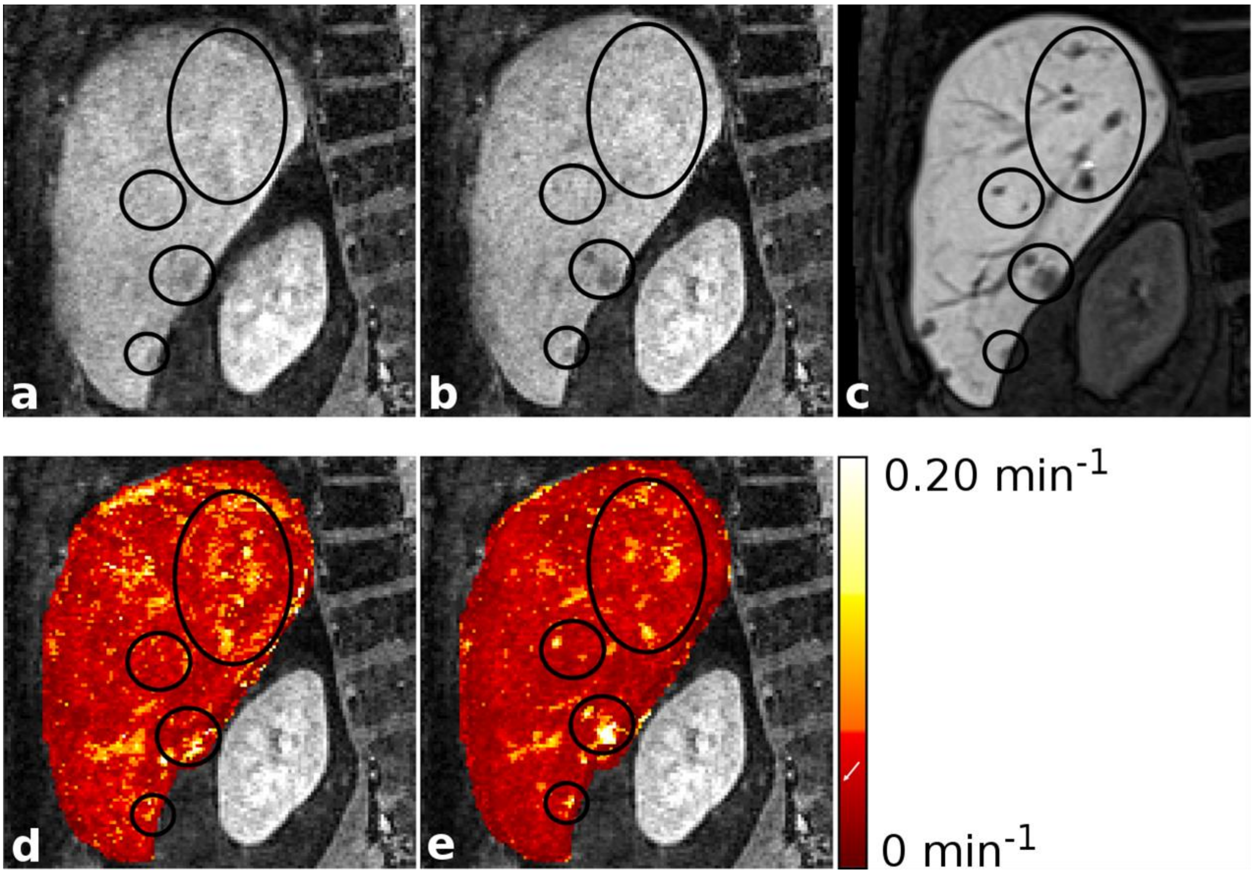

Figure 4: Coronal section of the liver depicting various metastases (black circles) and vessels. Images are: (a) NMC DCE$_f$, (b) MC DCE$_f$, (c) Turbo Spin Echo, (d) NMC K_{trans} map and (d) MC K_{trans} map. The presented figure was based on data published in (5).

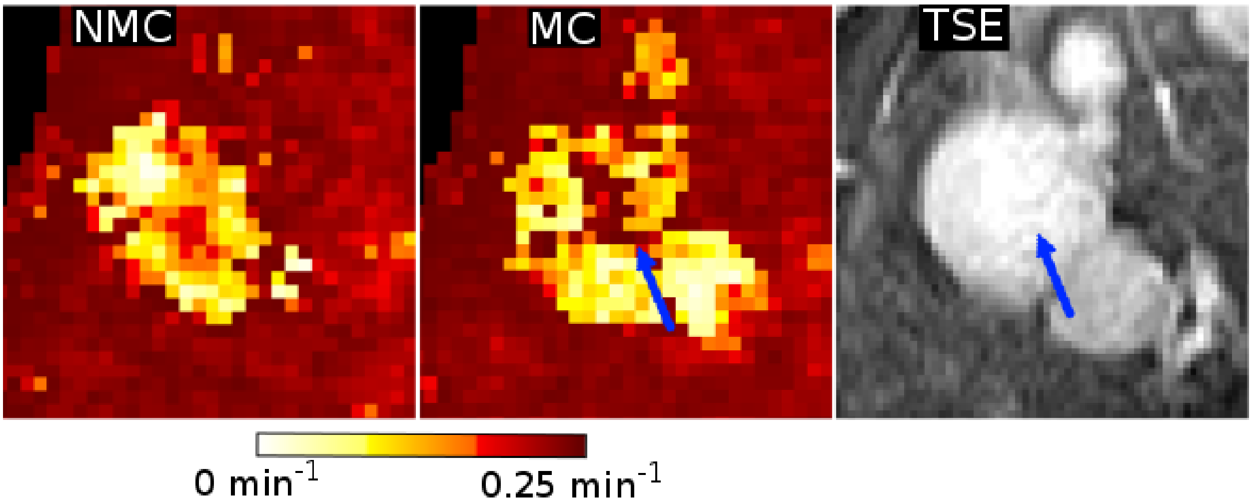

Figure 5: Axial section of necrotic core lesion, showing low permeability in its center (blue arrow). Images depict from left to right: NMC K_{trans} map, MC K_{trans} map and Turbo Spin Echo image used to confirm the presence of the necrotic core given by hyperintensity measured in its center. The presented figure was based on data published in (5).

4 - DISCUSSION

4.1 QSM

QSM in the brain is a very versatile novel tissue contrast mechanism that has found broad use in recent years, in a variety of different applications that include iron quantification for the investigation of neurodegenerative diseases and the detection of calcifications, hemorrages and some tumor types (6). In this work we first attempted to establish the level of correlation and reproducibility among QSM reconstructions of identical protocols, obtained through the MEDI algorithm (19, 20) at the field strenghts of 1.5T and 3T respectively. This step served two purposes: firstly to provide valuable information on the reproducibility of QSM recostructions with MEDI, specifically on the scanners and vendor employed, that could be exploited for comparative and multicenter studies; secondly, after the former point has been established, to verify reproducibility of QSM reconstructions within each field strength and by varying acquisition BW, with the scope of enhancing image contrast.

The evaluation of reproducibility and consistency across the two field strenghts demonstrated a very high degree of correlation ($R \geq 0.9$) between all four QMS reconstructions, already at the whole-brain voxelwise-level. Correlation for the ROI-based analysis was even higher ($R \geq 0.9$). This suggests that the MEDI algorithm in conjunction with the proposed SPGR protocols, is capable of yielding highly reproducible and consistent QSM reconstructions across different field strenghts. Similar findings were reported in the investigation of reproducubility and consistency of QSM measurements carried out within the same field strength and varying the BW ($R \geq 0.93$). In general the reproducibility evaluations, seem to advocate a certain degree of robustness of the QSM maps obtained with the MEDI algorithm, in response to acquisition BW variation and field strength used. This robustness can be exploited in case of BW variation to enhance the image contrast over structures sensible to such variation (up to 25% increase in caudate nucleus), while ensuring reconstruction of stable and consistent QSM maps. This feature would in principle facilitate the design of multicenter and comparative QSM studies to be used for several different applications, meanwhile permitting the continued use of 1.5T scanners, which still make up the vast majority of MR scanners in the clinical scenario.

Due to the large variety of combinations available between MR acquisition protocols, field strengths employed and QSM reconstruction frameworks, a direct comparison of QSM studies is often very challenging. However, similar studies to the presented work have investigated the reproducibility and consistency of QSM measurements deriving from SPGR protocols across 1.5T and 3T scanners, both with the MEDI algorithm (24) and with different algorithms (23). All results seem to indicate a very good level of correlation across the employed field strengths and also across the different algorithms employed, suggesting that the presented and other examined frameworks are sufficiently robust to converge to comparable results. In this study, the variability found in the comparisons among QSM maps can be ascribed only to the variation in field strength and to the variation of the acquisition bandwidth, separately. Furthermore, voxel size and matrix size were also kept constant across protocols in order to ensure this assumption.

The main reasons for choosing bandwidth as the viable acquisition parameter to be varied for this study, lie in the relationship that it has with SNR and sampled noise. Infact, bandwidth is inversely proportional to SNR and directly proportional to the sampling time. Therefore increasing the bandwidth reduces the SNR and increases the amount of sampled noise, allowing in principle to: probe shorter TEs which are used to detect tissues characterized by strong susceptibilities (11); increase the number of available echoes in multi-echo GRE (and SPGR), which affect the range of available tissues to probe and also aid in the estimation of the field map by increasing the number of available phase points to be fitted (14); help reduce the susceptibility artefacts that are directly proportional to the TE employed and inversely proportional to the acquisition bandwidth (34). For the above reasons it was therefore expected to be able to observe changes in QSM image quality by introducing bandwidth variation and a good compromise was sought between gain in SNR and scan time increase.

The presented work represents a first step towards enhancement in QSM image quality, obtainable through the optimization of the acquisition bandwidth for the introduced SPGR protocol acquired at 1.5T and post-processed by the MEDI algorithm. Several additional sequence parameters and QSM reconstruction algorithms still need to be investigated in combination, in order to further enhance QSM image quality and quantitativity and will be the object of follow up studies. Effects on the implemented evaluations, derived from increasing spatial resolution ($0.8 \times 0.8 \times 1.5$ mm^3) and varying the regularization parameter ($\lambda = 316$) have also been tested, resulting in good agreement with previous findings.

4.2 Motion Correction

Respiratory motion correction is a very powerful and helpful tool to be coupled with DCE-MR imaging to minimize respiratory motion artifacts, as it improves image quality and can aid in the detection of malignancies in DCE-MR images without depending on patient cooperation (e.g.

breathholding). Furthermore, it can enhance the diagnostic power of the technique by providing accurate maps of functional parameters to be employed as potential additional biomarkers (44).

The improved alignment among the 48 DCE phases and the improved AIF sampling especially over the peak of enhancement, ensured that contamination in the signal coming from surrounding tissue was prevented as is shown in Figure 3, while also ensuring that K_{trans} was not overestimated, increasing the comparability among different subjects and facilitating potential group studies. Figure 4 specifically shows how motion correction enhanced contrast over lesions and other small structures characterised by high permeability such as vessels, in K_{trans} maps. This effect can be attributed to the benefits brought to the model fitting procedure by the above-mentioned increased DCE-MR image alignment in time and space, the improved AIF sampling and the high temporal sampling. As a consequence, functional maps of permeability could clearly reveal the presence of structures even when these were not as well visible in the respective MC DCE_f images due to residual blurring from respiratory motion in the single selected time-point. The reduced blurring present in all MC images improved lesion delineation in terms of size and sharpness of contours and most importantly, when examining permeability maps, it allowed in some instances to see small lesions which were completely absent in the NMC data, as was also confirmed by Turbo Spin Echo images. In addition, Figure 5 shows how motion correction increased sensitivity in permeability maps, aiding in identifying the presence of necrotic core tumors, whose presence was also confirmed by the Turbo Spin Echo images. This is allowed by the reduction in image blurring among all the DCE phases composing a timeseries. The successful alignment among the different DCE-MR phases and the removal of the motion artifacts has therefore improved the CNR of the resulting K_{trans} maps significantly by 62% and that of late DCE images by 47%.

Other recent studies (38, 41) have also attempted to perform deformable respiratory motion correction of the liver. In (38) DCE-MR data is acquired through a stack-of-stars sequence that separates the dynamics in two extra dimensions representing contrast-enhancement and respiration respectively. On the other hand, the through-plane spatial resolution is over three times larger than for the presented framework. Analogous resolution considerations hold for the approach presented in (41), where motion correction is carried as a post-processing step rather than during image reconstruction. The main factor responsible for the increase in the overall spatial and temporal resolution observed in the presented work, is the GRPE sequence used in combination with the kt-SENSE reconstruction, which is particularly robust against undersampling allowing for the needed resolution flexibility (49). In other words, the use of this type of sequence has permitted to tune the balance needed between temporal and spatial resolution, overcoming for this particular instance the problem generally associated with reaching sufficient SNR in fast acquisition techniques, thanks to the robustness against undersampling characteristic of this sequence.

Through the proposed motion correction framework, it was possible to obtain MFs that yielded DCE images and functional maps with higher quality and contrast of hepatic metastases and other features of interest (ie. cysts, hemangiomas and necrotic core tumors) with respect to uncorrected images. Respiratory motion artifacts were successfully removed in data acquired during free-breathing, while preserving information on the MR contrast agent and at the same time providing DCE-MR images with high isotropic spatial resolution (1.5 mm) and good image quality. Furthermore, this framework could in principle be applied to correct for any organ motion comprising the abdomen, provided the organ in question shows sufficient contrast uptake signal in the dynamic frames, in order to be able to estimate respiratory motion (58).

Currently, further studies are being carried out in order to extend the presented motion correction framework to PET data simultaneously acquired with the DCE-MR on a hybrid PET-MR scanner. The aim of further developing such a framework is to be able to provide complementary information (ie. morpholigical, functional/metabolic), that are well aligned to each other and with individually increased levels of image contrast, providing a potential tool for a comprehensive evaluation of hepatic lesions. A qualitative example showing the improved image quality for both PET and MR parameters is reported in Figure 6, where a hepatic lesion is shown in motion corrected and uncorrected images.

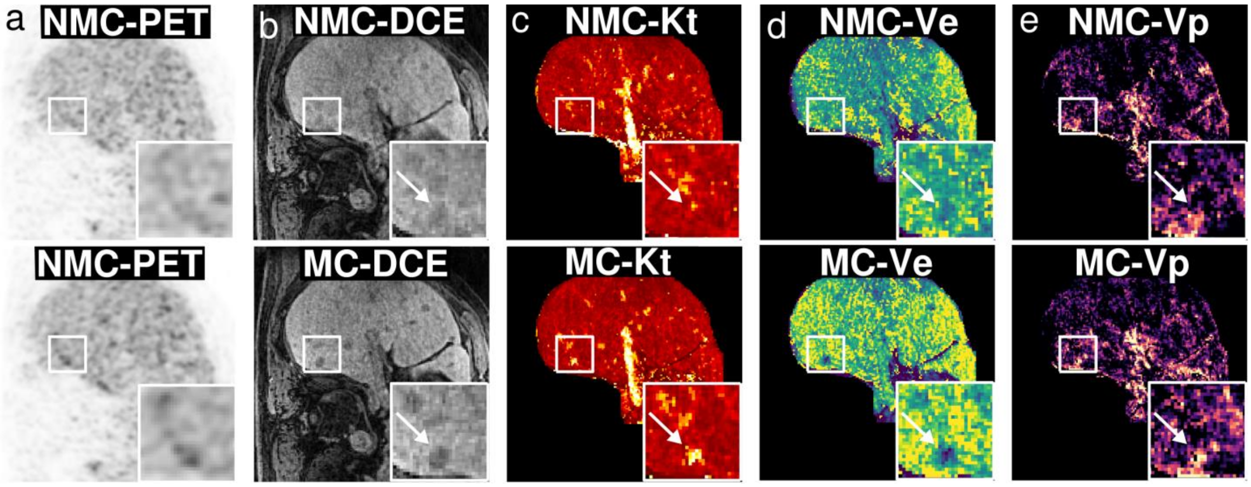

Figure 6: Axial section of a liver with close-up on small hepatic lesion (white arrows), depicting motion-corrected (bottom row) and uncorrected (top row) images of PET (a), DCE-MR late phase (b), K_{trans} (c), v_e (d) and v_p (d). Motion-corrected and uncorrected images of the same quantities, share the same scale in order to enable direct visual comparison. The presented figure was partly based on data published in (5).

Future improvements of this method may focus on the employment of Deep Learning methods to reduce the time required for carrying out motion correction during image reconstruction and fitting of the pharmacokinetic model (59). The long reconstruction time required to obtain the quantitative DCE parameters can be currently considered the main technical limitation in order to foster integration in the clinical setting. Lastly, in order to further verify the effects of the presented motion correction framework on the image contrasts that can be derived from PET and DCE-MR data and to robustly investigate the classification potential on the lesions, large clinical trials adopting also histopathology should be established. More specific and advanced hepatic models, which require the hepatic artery for sampling the AIF should also be investigated (60).

5 - CONCLUSION

In this synopsis, an acquisition protocol designed to optimize CNR in QSM reconstructions and a 3D non-rigid motion correction framework for DCE-MR have been presented, in the context of developing and optimizing methods for quantitative MRI apt at generating image contrasts which can be used as biomarkers.

Concerning QSM, correlation of measurements obtained between the clinical field strengths of 1.5T and 3T have been verified and compared to that of available similar studies, indicating a high level of consistency and reproducibility of measurements across field strengths. Moreover, bandwidth variations in the SPGR acquisition protocol have been tested to derive an optimal setting, for enhancing contrast in QSM images of the brain reconstructed from 1.5T acquisitions. Specifically, the lowest bandwidth sequence yielded a 25% increase in CNR over the caudate nucleus with respect to the highest bandwidth sequence. This result demonstrated the feasibility of increasing image contrast in final QSM reconstructions over features of interest in the brain for a negligible increase in scan time on the clinically most commonly available 1.5T scanners.

Regarding Motion Correction, a framework has been developed to carry out free-breathing 3D non-rigid motion corrected DCE-MR of the abdomen with isotropic spatial resolution of 1.5 mm. The approach uses all acquired data in the reconstruction of the DCE-MR series and derives all necessary motion information from it. CNR has been increased by 47% and 62% in late DCE-MR images and endothelial permeability maps respectively. The motion artifact suppression and accurate image realignment achieved by the proposed framework have shown to yield higher quality DCE-MR and functional images that can detect lesions and features of interest such as necrotic structures in cases where they would otherwise be missed, making it a viable tool for aiding and improving clinical diagnosis.

6 – REFERENCES

1. Vergeldt FJ, Prusova A, Fereidouni F, van Amerongen H, Van As H, Scheenen TWJ, Bader AN. Multi-component quantitative magnetic resonance imaging by phasor representation. Sci Rep. 2017; 7: 861.
2. Deng J, Wang Y. Quantitative magnetic resonance imaging biomarkers in oncological clinical trials: Current techniques and standardization challenges. Chronic Dis Transl Med. 2017 Mar 11;3(1):8-20.
3. Rosenkrantz AB, Mendiratta-Lala M, Bartholmai BJ, Ganeshan D, Abramson RG, Burton KR, Yu JP, Scalzetti EM, Yankeelov TE, Subramaniam RM, Lenchik L. Clinical utility of quantitative imaging. Acad Radiol. 2015;22(1):33-49.
4. Ippoliti M, Adams LC, Brenner W, Hamm B, Spincemaille P, Wang Y, Makowski MR. Quantitative susceptibility mapping across two clinical field strengths: Contrast-to-noise ratio enhancement at 1.5T. J Magn Reson Imaging. 2018 Nov;48(5):1410-1420.
5. Ippoliti M, Lukas M, Brenner W, Schaeffter T, Makowski MR, Kolbitsch C. 3D nonrigid motion correction for quantitative assessment of hepatic lesions in DCE-MRI. Magn Reson Med. 2019 Nov;82(5):1753-1766.
6. Deistung A, Schweser F, Reichenbach JR. Overview of quantitative susceptibility mapping. NMR Biomed 2017;30:e3569.
7. Schenck JF. The role of magnetic susceptibility in magnetic resonance imaging: MRI magnetic compatibility of the first and second kinds. Med. Phys. 1996; 23(6): 815–850.
8. Reichenbach JR, Venkatesan R, Yablonskiy DA, Thompson MR, Lai S, Haacke EM. Theory and application of static field inhomogeneity effects in gradient-echo imaging. J. Magn. Reson. Imaging 1997; 7(2): 266–279.
9. Jezzard P, Clare S. Sources of distortion in functional MRI data. Hum. Brain Mapp. 1999; 8(2–3): 80–85.
10. Haacke EM, Liu S, Buch S, Zheng W, Wu D, Ye Y. Quantitative susceptibility mapping: current status and future directions. Magn Reson Imaging 2015;33:1-25.
11. Wang Y, Liu T. Quantitative susceptibility mapping (QSM): Decoding MRI data for a tissue magnetic biomarker. Magn Reson Med 2015;73:82-101.
12. Haacke EM, Brown RW, Thompson MR, Venkatesan R. Magnetic properties of tissues: theory and measurements. In Magnetic Resonance Imaging – Physical Principles and Sequence Design, 1st edn. John Wiley & Sons. 1999;741–780.

13. Sun H, Wilman AH. Quantitative susceptibility mapping using single-shot echo-planar imaging. Magn. Reson. Med. 2015*;* 73*(*5*):* 1932–1938.
14. Kressler B, de Rochefort L, Liu T, Spincemaille P, Jiang Q, Wang Y. Nonlinear regularization for per voxel estimation of magnetic susceptibility distributions from MRI field maps. IEEE Trans Med Imaging 2010;29:273-281.
15. Wu B, Li W, Avram AV, Gho SM, Liu C. Fast and tissue-optimized mapping of magnetic susceptibility and T2* with multi-echo and multi-shot spirals. Neuroimage 2012*;* 59*(*1*):* 297–305.
16. Liu T, Wisnieff C, Lou M, Chen W, Spincemaille P, Wang Y. Nonlinear formulation of the magnetic field to source relationship for robust quantitative susceptibility mapping. Magn. Reson. Med. 2013; 69(2): 467–476.
17. Langkammer C, Bredies K, Poser BA, Barth M, Reishofer G, Fan AP, Bilgic B, Fazekas F, Mainero C, Ropele S. Fast quantitative susceptibility mapping using 3D EPI and total generalized variation. Neuroimage 2015*;* 111*:* 622–630.
18. Yeo DT, Fessler JA, Kim B. Motion robust magnetic susceptibility and field inhomogeneity estimation using regularized image restoration techniques for fMRI. Med Image Comput Assist Interv 2008;11:991–998.
19. de Rochefort L, Liu T, Kressler B, Liu J, Spincemaille P, Lebon V, Wu J, Wang Y.. Quantitative susceptibility map reconstruction from MR phase data using bayesian regularization: validation and application to brain imaging. Magn Reson Med 2010;63:194-206.
20. Liu J, Liu T, de Rochefort L, Ledoux J, Khalidov I, Chen W, Tsiouris AJ, Wisnieff C, Spincemaille P, Prince MR, Wang Y. Morphology enabled dipole inversion for quantitative susceptibility mapping using structural consistency between the magnitude image and the susceptibility map. NeuroImage 2012;59:2560-2568.
21. Li W, Wu B, Liu C. Quantitative susceptibility mapping of human brain reflects spatial variation in tissue composition. NeuroImage 2011;55:1645-1656.
22. Xu B, Spincemaille P, Liu T, Prince MR, Dutruel S, Gupta A, Thimmappa ND, Wang Y. Quantification of cerebral perfusion using dynamic quantitative susceptibility mapping. Magn Reson Med 2015;73:1540-1548.
23. Hinoda T, Fushimi Y, Okada T, Fujimoto K, Liu C, Yamamoto A, Okada T, Kido A, Togashi K. Quantitative Susceptibility Mapping at 3 T and 1.5 T: Evaluation of Consistency and Reproducibility. Invest Radiol 2015;50:522-530.

24. Deh K, Nguyen TD, Eskreis-Winkler S, Prince MR, Spincemaille P, Gauthier S, Kovanlikaya I, Zhang Y, Wang Y. Reproducibility of quantitative susceptibility mapping in the brain at two field strengths from two vendors. J Magn Reson Imaging 2015;42:1592–1600.
25. Edelstein WA, Glover GH, Hardy CJ, Redington RW. The intrinsic signal-to-noise ratio in NMR imaging. Magn Reson Med. 1986;3:604–18.
26. Wardlaw JM, Brindle W, Casado AM, Shuler K, Henderson M, Thomas B, Macfarlane J, Maniega SM, Lymer K, Morris Z, Pernet C, Nailon W, Ahearn T, Mumuni AN, Mugruza C, McLean J, Chakirova G, Tao YT, Simpson J, Stanfield AC, Johnston H, Parikh J, Royle NA, De Wilde J, Bastin ME, Weir N, Farrall A, Valdes Hernandez MC & The SINAPSE Collaborative Group. A systematic review of the utility of 1.5 versus 3 Tesla magnetic resonance brain imaging in clinical practice and research. Eur Radiol 2012;22:2295–2303.
27. Sarracanie M, LaPierre CD, Salameh N, Waddington DE, Witzel T, Rosen MS. Low-cost high-performance MRI. Sci Rep 2015;5:15177.
28. Port JD, Pomper MG. Quantification and minimization of magnetic susceptibility artifacts on GRE images. J Comput Assist Tomogr 2000;24:958-964.
29. Choyke PL, Dwyer AJ, Knopp MV. Functional tumor imaging with dynamic contrast-enhanced magnetic resonance imaging. J Magn Reson Imag 2003;17:509–520.
30. Padhani AR. Dynamic contrast-enhanced MRI studies in human tumours. Br J Radiol. 1999;72:427–431.
31. Padhani AR. Dynamic contrast-enhanced MRI in clinical oncology: current status and future directions. J Magn Reson Imaging. 2002;16:407–422
32. Tofts PS, Brix G, Buckley DL, Evelhoch JL, Henderson E, Knopp MV, Larsson HB, Lee TY, Mayr NA, Parker GJ, Port RE, Taylor J, Weisskoff RM. Estimating kinetic parameters from dynamic contrast-enhanced T(1)-weighted MRI of a diffusable tracer: standardized quantities and symbols. J Magn Reson Imaging 1999;10:223–232.
33. Miyazaki K, Orton MR, Davidson RL, d'Arcy JA, Lewington V, Koh TS, Thng CH, Leach MO, Collins DJ, Koh DM. Neuroendocrine tumor liver metastases: use of dynamic contrast-enhanced MR imaging to monitor and predict radiolabeled octreotide therapy response. Radiology 2012;263:139–148.
34. Melbourne A, Atkinson D, White MJ, Collins D, Leach M, Hawkes D. Registration of dynamic contrast-enhanced MRI using a progressive principal component registration (PPCR). Phys Med Biol. 2007;52:5147–5156.

35. Bultman EM, Brodsky EK, Horng DE, Irarrazaval P, Schelman WR, Block WF, Reeder SB. Quantitative hepatic perfusion modeling using DCE-MRI with sequential breath-holds. J Magn Reson Imaging. 2014;39:853–865.
36. Reiner CS, Neville AM, Nazeer HK, Breault S, Dale BM, Merkle EM, Bashir MR. Contrast-enhanced free-breathing 3D T1-weighted gradient-echo sequence for hepatobiliary MRI in patients with breath-holding difficulties. Eur Radiol 2013;23:3087–93.
37. Feng L, Grimm R, Block KT, Chandarana H, Kim S, Xu J, Axel L, Sodickson DK, Otazo R. Golden-angle radial sparse parallel MRI: combination of compressed sensing, parallel imaging, and golden-angle radial sampling for fast and flexible dynamic volumetric MRI. Magn Reson Med. 2014 Sep;72(3):707-17.
38. Feng L, Axel L, Chandarana H, Block KT, Sodickson DK, Otazo R. XD-GRASP: golden-angle radial MRI with reconstruction of extra motion-state dimensions using compressed sensing. Magn Reson Med 2015;75:775–788.
39. Hamy V, Dikaios N, Punwani S, Melbourne A, Latifoltojar A, Makanyanga J, Chouhan M, Helbren E, Menys A, Taylor S, Atkinson D. Respiratory motion correction in dynamic MRI using robust data decomposition registration – application to DCE-MRI. Med Image Anal 2014;18:301–313.
40. Cheng JY, Zhang T, Ruangwattanapaisarn N, Alley MT, Uecker M, Pauly JM, Lustig M, Vasanawala SS. Free-breathing pediatric MRI with nonrigid motion correction and acceleration. J Magn Reson Imaging 2015;42:407–420.
41. Johannson A, Balter JM, Cao Y. Abdominal DCE-MRI reconstruction with deformable motion correction for liver perfusion quantification. Med Phys. 2018;45:4529–4540.
42. Lausch A, Ebrahimi M, Martel A. Image registration for abdominal dynamic contrast-enhanced magnetic resonance images. IEEE International Symposium on Biomedical Imaging: From Nano to Macro, Chicago, IL. 2011;561-565.
43. Kim H. Variability in Quantitative DCE-MRI: Sources and Solutions. J Nat Sci. 2018;4(1):e484.
44. Türkbey B, Thomasson D, Pang Y, Bernardo M, Choyke PL. The role of dynamic contrast-enhanced MRI in cancer diagnosis and treatment. Diagn Interv Radiol. 2010;16(3):186-192.
45. Jajamovich GH, Huang W, Besa C, Lin X, Afzal A, Dyvorne HA, Taouli B. DCE-MRI of hepatocellular carcinoma: perfusion quantification with Tofts model versus shutter-speed model—initial experience. Magn Reson Mater Phy. 2016;29:49–58.

46. Winkelmann S, Schaeffter T, Koehler T, Eggers H, Doessel O. An optimal radial profile order based on the golden ratio for time-resolved MRI. IEEE Trans Med Imaging 2007;26:68–76.
47. Friston KJ, Ashburner J, Kiebel SJ, Nichols TE. Statistical Parametric Mapping: The Analysis of Functional Brain Images. Academic Press 2006:656.
48. Jenkinson M, Beckmann CF, Behrens TE, Woolrich MW, Smith SM. Fsl. NeuroImage 2012;62:782-790.
49. Prieto C, Uribe S, Razavi R, Atkinson D, Schaeffter T. 3D Undersampled Golden-Radial Phase Encoding for DCE-MRA Using Inherently Regularized Iterative SENSE. Magn Reson Imaging 2010;64:514–526.
50. Buerger C, Prieto C, Schaeffter T. Highly efficient 3D motion-compensated abdomen MRI from undersampled golden-RPE acquisitions. Magma Magn Reson Mater Physics Biol Med 2013;26:419– 429.
51. Rueckert D, Sonoda LI, Hayes C, Hill DLG, Leach MO, Hawkes DJ. Nonrigid registration using free-form deformations: application to breast MR images. IEEE Trans Med Imaging 1999;18:712–721.
52. Cruz G, Atkinson D, Buerger C, Schaeffter T, Prieto C. Accelerated motion corrected three-dimensional abdominal MRI using total variation regularized SENSE reconstruction. Magn Reson Med 2016;75:1484–1498.
53. Tsao J, Boesiger P, Pruessmann KP. k-t BLAST and k-t SENSE: Dynamic MRI with high frame rate exploiting spatiotemporal correlations. Magn Reson Med 2003;50:1031–1042.
54. DCE MRI Technical Committee. DCE MRI Quantification Profile, Quantitative Imaging Biomarkers Alliance. Version 1.0. Reviewed Draft. QIBA, July 1, 2012. Available from: http://rsna.org/QIBA_.aspx
55. Medved M, Karczmar G, Yang C, Dignam J, Gajewski TF, Kindler H, Vokes E, MacEneany P, Mitchell MT, Stadler WM. Semiquantitative analysis of dynamic contrast enhanced MRI in cancer patients: variability and changes in tumor tissue over time. J Magn Reson Imaging 2004;20:122–128.
56. de Bazelaire CM, Duhamel GD, Rofsky NM, Alsop DC. MR imaging relaxation times of abdominal and pelvic tissues measured in vivo at 3.0 T: preliminary results. Radiol 2004;230: 652–659.
57. Rohrer M, Bauer H, Mintorovitch J, Requardt M, Weinmann HJ. Comparison of Magnetic Properties of MRI Contrast Media Solutions at Different Magnetic Field Strengths. Invest Radiol 2005;40:715–724.

58. Zöllner FG, Sance R, Rogelj P, Ledesma-Carbayo MJ, Rørvik J, Santos A, Lundervold A. Assessment of 3D DCE-MRI of the kidneys using non-rigid image registration and segmentation of voxel time courses. Comput Med Imaging Graph. 2009; 33(3):171–181.
59. Lundervold A, Lundervold A. An overview of deep learning in medical imaging focusing on MRI. Z Med Phys. 2019;29(2):102–107.
60. Yang JF, Zhao ZH, Zhang Y, Zhao L, Yang LM, Zhang MM, Wang BY, Wang T, Lu BC. Dual-input two-compartment pharmacokinetic model of dynamic contrast-enhanced magnetic resonance imaging in hepatocellular carcinoma. World J Gastroeneterol 2016;22:3652–3662.

Statutory Declaration

"**I**, Matteo Ippoliti, by personally signing this document in lieu of an oath, hereby affirm that I prepared the submitted dissertation on the topic "Development and optimization of methods for quantitative Magnetic Resonance Imaging: QSM and DCE-MR" ("Entwicklung und Optimierung von Methoden zur quantitativen Magnetresonanztomographie: QSM und DCE-MR"), independently and without the support of third parties, and that I used no other sources and aids than those stated.
All parts which are based on the publications or presentations of other authors, either in letter or in spirit, are specified as such in accordance with the citing guidelines. The sections on methodology (in particular regarding practical work, laboratory regulations, statistical processing) and results (in particular regarding figures, charts and tables) are exclusively my responsibility.

Furthermore, I declare that I have correctly marked all of the data, the analyses, and the conclusions generated from data obtained in collaboration with other persons, and that I have correctly marked my own contribution and the contributions of other persons (cf. declaration of contribution). I have correctly marked all texts or parts of texts that were generated in collaboration with other persons.

My contributions to any publications to this dissertation correspond to those stated in the below joint declaration made together with the supervisor. All publications created within the scope of the dissertation comply with the guidelines of the ICMJE (International Committee of Medical Journal Editors; www.icmje.org) on authorship. In addition, I declare that I shall comply with the regulations of Charité – Universitätsmedizin Berlin on ensuring good scientific practice.

I declare that I have not yet submitted this dissertation in identical or similar form to another Faculty.

The significance of this statutory declaration and the consequences of a false statutory declaration under criminal law (Sections 156, 161 of the German Criminal Code) are known to me."

Date Signature

Declaration of your own contribution to the top-journal publication for a PhD or MD/PhD degree

Matteo Ippoliti contributed the following to the below listed publications:

Publication 1: Ippoliti, M., Adams, L.C., Winfried, B., Hamm, B., Spincemaille, P., Wang, Y. and Makowski, M.R. Quantitative susceptibility mapping across two clinical field strengths: Contrast-to-noise ratio enhancement at 1.5T. Journal of Magnetic Resonance Imaging. 2018

Contribution:

- SPGR sequence protocol optimization for MRI data acquisition on all scanners (Ippoliti);
- MRI data acquisition of healthy volunteers (Ippoliti);
- Data preparation, processing and analysis (Ippoliti);
- Establishment and implementation of methods (Ippoliti);
- Statistical and CNR analyses for quantitative image evaluations (Ippoliti);
- Evaluation of QSM maps image quality (Adams, Ippoliti, Makowski);
- Manuscript creation including all text, figures and tables (Ippoliti)

Publication 2: Ippoliti, M., Lukas, M., Brenner, W., Schaeffter, T., Makowski, M.R., Kolbitsch, C. 3D nonrigid motion correction for quantitative assessment of hepatic lesions in DCE-MRI. Magnetic Resonance in Medicine. 2019

Contribution:

- GRPE sequence protocol compilation and implementation for MRI data acquisition on Biograph mMR scanner (Ippoliti);
- MRI data acquisition and raw data extraction and handling of included subjects (Ippoliti);
- MR image reconstruction for MF derivation and for final motion-corrected image reconstruction of DCE-MR image time-series (Ippoliti);
- Data preparation, processing and analysis (Ippoliti);
- Establishment and implementation of methods (Ippoliti);
- Statistical and CNR analyses for quantitative image evaluations (Ippoliti);
- Manuscript creation including all text, figures and tables (Ippoliti)

____

Signature, date and stamp of first supervising university professor / lecturer

____

Signature of doctoral candidate

Journal Data Filtered By: **Selected JCR Year: 2016** Selected Editions: SCIE,SSCI Selected Categories: **“RADIOLOGY, NUCLEAR MEDICINE and MEDICAL IMAGING”** Selected Category Scheme: WoS

Gesamtanzahl: 126 Journale

Rank	Full Journal Title	Total Cites	Journal Impact Factor	Eigenfactor Score
1	JACC-Cardiovascular Imaging	6,895	10.189	0.027050
2	RADIOLOGY	50,983	7.296	0.066140
3	EUROPEAN JOURNAL OF NUCLEAR MEDICINE AND MOLECULAR IMAGING	14,019	7.277	0.024910
4	Circulation-Cardiovascular Imaging	4,472	6.803	0.019120
5	JOURNAL OF NUCLEAR MEDICINE	24,977	6.646	0.037540
6	NEUROIMAGE	85,630	5.835	0.173210
7	JOURNAL OF CARDIOVASCULAR MAGNETIC RESONANCE	4,349	5.601	0.014950
8	SEMINARS IN RADIATION ONCOLOGY	2,232	5.356	0.003910
9	INVESTIGATIVE RADIOLOGY	5,925	5.195	0.011230
10	INTERNATIONAL JOURNAL OF RADIATION ONCOLOGY BIOLOGY PHYSICS	44,068	5.133	0.060060
11	ULTRASOUND IN OBSTETRICS & GYNECOLOGY	11,611	4.710	0.019350
12	HUMAN BRAIN MAPPING	18,139	4.530	0.041900
13	RADIOTHERAPY AND ONCOLOGY	15,639	4.328	0.028040
14	MEDICAL IMAGE ANALYSIS	5,539	4.188	0.010720
15	EUROPEAN RADIOLOGY	16,381	3.967	0.033340
16	IEEE TRANSACTIONS ON MEDICAL IMAGING	15,215	3.942	0.019660
17	JOURNAL OF NUCLEAR CARDIOLOGY	3,021	3.930	0.003920
18	MAGNETIC RESONANCE IN MEDICINE	29,816	3.924	0.035960
19	CLINICAL NUCLEAR MEDICINE	4,008	3.640	0.006470
20	SEMINARS IN NUCLEAR MEDICINE	2,056	3.630	0.002800
21	AMERICAN JOURNAL OF NEURORADIOLOGY	21,720	3.550	0.032180
22	MOLECULAR IMAGING AND BIOLOGY	2,228	3.466	0.005880
23	ULTRASCHALL IN DER MEDIZIN	1,907	3.452	0.003930
24	RADIOGRAPHICS	10,286	3.427	0.009660
25	Biomedical Optics Express	6,187	3.337	0.021610
26	Contrast Media & Molecular Imaging	1,131	3.307	0.002810
27	INTERNATIONAL JOURNAL OF HYPERTHERMIA	3,030	3.262	0.003810

Rank	Full Journal Title	Total Cites	Journal Impact Factor	Eigenfactor Score
28	Journal of Cardiovascular Computed Tomography	1,331	3.185	0.004220
29	JOURNAL OF MAGNETIC RESONANCE IMAGING	15,073	3.083	0.029170
30	Journal of the American College of Radiology	2,690	2.993	0.006840
31	NMR IN BIOMEDICINE	6,766	2.872	0.014560
32	JOURNAL OF VASCULAR AND INTERVENTIONAL RADIOLOGY	8,371	2.780	0.012840
33	AMERICAN JOURNAL OF ROENTGENOLOGY	31,676	2.778	0.035740
34	PHYSICS IN MEDICINE AND BIOLOGY	22,873	2.742	0.034390
35	STRAHLENTHERAPIE UND ONKOLOGIE	2,687	2.735	0.004990
36	Clinical Neuroradiology	433	2.618	0.001550
37	MEDICAL PHYSICS	22,942	2.617	0.037250
38	Radiation Oncology	4,358	2.568	0.013680
39	RADIATION RESEARCH	8,394	2.539	0.007920
40	JOURNAL OF BIOMEDICAL OPTICS	12,700	2.530	0.024520
41	JOURNAL OF NEURORADIOLOGY	792	2.526	0.001310
42	ULTRASOUND IN MEDICINE AND BIOLOGY	9,759	2.494	0.012640
43	QUARTERLY JOURNAL OF NUCLEAR MEDICINE AND MOLECULAR IMAGING	1,030	2.481	0.001800
44	CLINICAL RADIOLOGY	5,717	2.478	0.008540
45	EUROPEAN JOURNAL OF RADIOLOGY	11,328	2.462	0.026500
46	NUCLEAR MEDICINE AND BIOLOGY	3,918	2.426	0.006210
47	CANCER IMAGING	1,008	2.404	0.001930
48	RADIATION AND ENVIRONMENTAL BIOPHYSICS	1,468	2.398	0.002460
49	ULTRASONICS	5,752	2.327	0.008130
50	Diagnostic and Interventional Imaging	957	2.277	0.002420
51	MAGNETIC RESONANCE IMAGING	6,465	2.225	0.011370
52	CARDIOVASCULAR AND INTERVENTIONAL RADIOLOGY	4,859	2.191	0.008890
53	KOREAN JOURNAL OF RADIOLOGY	1,941	2.156	0.003730
54	ACADEMIC RADIOLOGY	4,804	2.128	0.009150
55	NEURORADIOLOGY	5,191	2.093	0.007520
56	Dose-Response	671	2.088	0.001310
57	Brachytherapy	1,442	2.082	0.003540
58	BRITISH JOURNAL OF RADIOLOGY	7,990	2.050	0.011760
59	EJNMMI Research	844	2.033	0.003380

Selected JCR Year: 2016; Selected Categories: “RADIOLOGY, NUCLEAR MEDICINE and MEDICAL IMAGING”

Ippoliti M, Adams LC, Brenner W, Hamm B, Spincemaille P, Wang Y, Makowski MR. Quantitative susceptibility mapping across two clinical field strengths: Contrast-to-noise ratio enhancement at 1.5T. *J Magn Reson Imaging*. 2018; 48: 1410-1420.

https://doi.org/10.1002/jmri.26045

Ippoliti M, Adams LC, Brenner W, Hamm B, Spincemaille P, Wang Y, Makowski MR. Quantitative susceptibility mapping across two clinical field strengths: Contrast-to-noise ratio enhancement at 1.5T. *J Magn Reson Imaging*. 2018; 48: 1410-1420.

https://doi.org/10.1002/jmri.26045

Ippoliti M, Adams LC, Brenner W, Hamm B, Spincemaille P, Wang Y, Makowski MR. Quantitative susceptibility mapping across two clinical field strengths: Contrast-to-noise ratio enhancement at 1.5T. *J Magn Reson Imaging*. 2018; 48: 1410-1420.

https://doi.org/10.1002/jmri.26045

Ippoliti M, Adams LC, Brenner W, Hamm B, Spincemaille P, Wang Y, Makowski MR. Quantitative susceptibility mapping across two clinical field strengths: Contrast-to-noise ratio enhancement at 1.5T. *J Magn Reson Imaging*. 2018; 48: 1410-1420.

https://doi.org/10.1002/jmri.26045

Ippoliti M, Adams LC, Brenner W, Hamm B, Spincemaille P, Wang Y, Makowski MR. Quantitative susceptibility mapping across two clinical field strengths: Contrast-to-noise ratio enhancement at 1.5T. *J Magn Reson Imaging*. 2018; 48: 1410-1420.

https://doi.org/10.1002/jmri.26045

Ippoliti M, Adams LC, Brenner W, Hamm B, Spincemaille P, Wang Y, Makowski MR. Quantitative susceptibility mapping across two clinical field strengths: Contrast-to-noise ratio enhancement at 1.5T. *J Magn Reson Imaging*. 2018; 48: 1410-1420.

https://doi.org/10.1002/jmri.26045

Ippoliti M, Adams LC, Brenner W, Hamm B, Spincemaille P, Wang Y, Makowski MR. Quantitative susceptibility mapping across two clinical field strengths: Contrast-to-noise ratio enhancement at 1.5T. *J Magn Reson Imaging*. 2018; 48: 1410-1420.

https://doi.org/10.1002/jmri.26045

Ippoliti M, Adams LC, Brenner W, Hamm B, Spincemaille P, Wang Y, Makowski MR. Quantitative susceptibility mapping across two clinical field strengths: Contrast-to-noise ratio enhancement at 1.5T. *J Magn Reson Imaging*. 2018; 48: 1410-1420.

https://doi.org/10.1002/jmri.26045

Ippoliti M, Adams LC, Brenner W, Hamm B, Spincemaille P, Wang Y, Makowski MR. Quantitative susceptibility mapping across two clinical field strengths: Contrast-to-noise ratio enhancement at 1.5T. *J Magn Reson Imaging*. 2018; 48: 1410-1420.

https://doi.org/10.1002/jmri.26045

Ippoliti M, Adams LC, Brenner W, Hamm B, Spincemaille P, Wang Y, Makowski MR. Quantitative susceptibility mapping across two clinical field strengths: Contrast-to-noise ratio enhancement at 1.5T. *J Magn Reson Imaging*. 2018; 48: 1410-1420.

https://doi.org/10.1002/jmri.26045

Ippoliti M, Adams LC, Brenner W, Hamm B, Spincemaille P, Wang Y, Makowski MR. Quantitative susceptibility mapping across two clinical field strengths: Contrast-to-noise ratio enhancement at 1.5T. *J Magn Reson Imaging*. 2018; 48: 1410-1420.

https://doi.org/10.1002/jmri.26045

Journal Data Filtered By: **Selected JCR Year: 2017** Selected Editions: SCIE,SSCI Selected Categories: **“RADIOLOGY, NUCLEAR MEDICINE and MEDICAL IMAGING”** Selected Category Scheme: WoS

Gesamtanzahl: 128 Journale

Rank	Full Journal Title	Total Cites	Journal Impact Factor	Eigenfactor Score
1	JACC-Cardiovascular Imaging	8,104	10.247	0.026360
2	European Heart Journal-Cardiovascular Imaging	4,630	8.336	0.020640
3	EUROPEAN JOURNAL OF NUCLEAR MEDICINE AND MOLECULAR IMAGING	14,983	7.704	0.024870
4	RADIOLOGY	54,109	7.469	0.063710
5	JOURNAL OF NUCLEAR MEDICINE	27,101	7.439	0.037560
6	CLINICAL NUCLEAR MEDICINE	4,756	6.281	0.006950
7	INVESTIGATIVE RADIOLOGY	6,486	6.224	0.012410
8	Circulation-Cardiovascular Imaging	5,438	6.221	0.020160
9	IEEE TRANSACTIONS ON MEDICAL IMAGING	17,837	6.131	0.024200
10	ULTRASOUND IN OBSTETRICS & GYNECOLOGY	12,420	5.654	0.018820
11	INTERNATIONAL JOURNAL OF RADIATION ONCOLOGY BIOLOGY PHYSICS	46,595	5.554	0.055060
12	JOURNAL OF CARDIOVASCULAR MAGNETIC RESONANCE	4,918	5.457	0.013530
13	NEUROIMAGE	92,719	5.426	0.152610
14	MEDICAL IMAGE ANALYSIS	6,383	5.356	0.011900
15	RADIOTHERAPY AND ONCOLOGY	17,184	4.942	0.027840
16	HUMAN BRAIN MAPPING	20,334	4.927	0.042810
17	SEMINARS IN NUCLEAR MEDICINE	2,285	4.558	0.002990
18	ULTRASCHALL IN DER MEDIZIN	2,201	4.389	0.004310
19	MAGNETIC RESONANCE IN MEDICINE	31,440	4.082	0.034130
20	EUROPEAN RADIOLOGY	18,615	4.027	0.034120
20	SEMINARS IN RADIATION ONCOLOGY	2,480	4.027	0.003620
22	JOURNAL OF NUCLEAR CARDIOLOGY	3,508	3.847	0.004120
23	AMERICAN JOURNAL OF NEURORADIOLOGY	22,667	3.653	0.029840
24	JOURNAL OF MAGNETIC RESONANCE IMAGING	16,398	3.612	0.027440
25	MOLECULAR IMAGING AND BIOLOGY	2,415	3.608	0.005480

Ippoliti M, Lukas M, Brenner W, Schaeffter T, Makowski MR, Kolbitsch C. 3D nonrigid motion correction for quantitative assessment of hepatic lesions in DCE-MRI. *Magn Reson Med*. 2019; 00: 1–14.

https://doi.org/10.1002/mrm.27867

Ippoliti M, Lukas M, Brenner W, Schaeffter T, Makowski MR, Kolbitsch C. 3D nonrigid motion correction for quantitative assessment of hepatic lesions in DCE-MRI. *Magn Reson Med*. 2019; 00: 1–14.

https://doi.org/10.1002/mrm.27867

Ippoliti M, Lukas M, Brenner W, Schaeffter T, Makowski MR, Kolbitsch C. 3D nonrigid motion correction for quantitative assessment of hepatic lesions in DCE-MRI. *Magn Reson Med*. 2019; 00: 1–14.

https://doi.org/10.1002/mrm.27867

Ippoliti M, Lukas M, Brenner W, Schaeffter T, Makowski MR, Kolbitsch C. 3D nonrigid motion correction for quantitative assessment of hepatic lesions in DCE-MRI. *Magn Reson Med*. 2019; 00: 1–14.

https://doi.org/10.1002/mrm.27867

Ippoliti M, Lukas M, Brenner W, Schaeffter T, Makowski MR, Kolbitsch C. 3D nonrigid motion correction for quantitative assessment of hepatic lesions in DCE-MRI. *Magn Reson Med*. 2019; 00: 1–14.

https://doi.org/10.1002/mrm.27867

Ippoliti M, Lukas M, Brenner W, Schaeffter T, Makowski MR, Kolbitsch C. 3D nonrigid motion correction for quantitative assessment of hepatic lesions in DCE-MRI. *Magn Reson Med*. 2019; 00: 1–14.

https://doi.org/10.1002/mrm.27867

Ippoliti M, Lukas M, Brenner W, Schaeffter T, Makowski MR, Kolbitsch C. 3D nonrigid motion correction for quantitative assessment of hepatic lesions in DCE-MRI. *Magn Reson Med*. 2019; 00: 1–14.

https://doi.org/10.1002/mrm.27867

Ippoliti M, Lukas M, Brenner W, Schaeffter T, Makowski MR, Kolbitsch C. 3D nonrigid motion correction for quantitative assessment of hepatic lesions in DCE-MRI. *Magn Reson Med*. 2019; 00: 1–14.

https://doi.org/10.1002/mrm.27867

Ippoliti M, Lukas M, Brenner W, Schaeffter T, Makowski MR, Kolbitsch C. 3D nonrigid motion correction for quantitative assessment of hepatic lesions in DCE-MRI. *Magn Reson Med*. 2019; 00: 1–14.

https://doi.org/10.1002/mrm.27867

Ippoliti M, Lukas M, Brenner W, Schaeffter T, Makowski MR, Kolbitsch C. 3D nonrigid motion correction for quantitative assessment of hepatic lesions in DCE-MRI. *Magn Reson Med*. 2019; 00: 1–14.

https://doi.org/10.1002/mrm.27867

Ippoliti M, Lukas M, Brenner W, Schaeffter T, Makowski MR, Kolbitsch C. 3D nonrigid motion correction for quantitative assessment of hepatic lesions in DCE-MRI. *Magn Reson Med*. 2019; 00: 1–14.

https://doi.org/10.1002/mrm.27867

Ippoliti M, Lukas M, Brenner W, Schaeffter T, Makowski MR, Kolbitsch C. 3D nonrigid motion correction for quantitative assessment of hepatic lesions in DCE-MRI. *Magn Reson Med*. 2019; 00: 1–14.

https://doi.org/10.1002/mrm.27867

Ippoliti M, Lukas M, Brenner W, Schaeffter T, Makowski MR, Kolbitsch C. 3D nonrigid motion correction for quantitative assessment of hepatic lesions in DCE-MRI. *Magn Reson Med*. 2019; 00: 1–14.

https://doi.org/10.1002/mrm.27867

Ippoliti M, Lukas M, Brenner W, Schaeffter T, Makowski MR, Kolbitsch C. 3D nonrigid motion correction for quantitative assessment of hepatic lesions in DCE-MRI. *Magn Reson Med*. 2019; 00: 1–14.

https://doi.org/10.1002/mrm.27867

Curriculum Vitae

My curriculum vitae does not appear in the electronic version of my paper for reasons of data protection.

Publication List

PUBLICATIONS IN PEER-REVIEWED SCIENTIFIC JOURNALS

1. **Ippoliti M**, Lukas M, Brenner W, Schaeffter T, Makowski MR, Kolbitsch C. 3D nonrigid motion correction for quantitative assessment of hepatic lesions in DCE-MRI. *Magn Reson Med*. 2019; 00: 1–14. https://doi.org/10.1002/mrm.27867.
2. **Ippoliti M**, Adams LC, Brenner W, Hamm B, Spincemaille P, Wang Y, Makowski MR. Quantitative susceptibility mapping across two clinical field strengths: Contrast-to-noise ratio enhancement at 1.5T. *J Magn Reson Imaging*. 2018; 48: 1410-1420. https://doi.org/10.1002/jmri.26045
3. Spincemaille P, Liu Z, Zhang S, Kovanlikaya I, **Ippoliti M**, Makowski M, Watts R, de Rochefort L, Venkatraman V, Desmond P, Santin MD, Lehéricy S, Kopell BH, Péran P, Wang Y. Clinical Integration of Automated Processing for Brain Quantitative Susceptibility Mapping: Multi-Site Reproducibility and Single-Site Robustness. *J Neuroimaging.* 2019; 0:1–10. https://doi.org/10.1111/jon.12658
4. **Ippoliti M**, Lukas M, Brenner W, Schatka I, Furth C, Schaeffter T, Makowski MR, Kolbitsch C. Respiratory motion correction for enhanced quantification of hepatic lesions in simultaneous PET and DCE-MR imaging. *Phys. Med. Biol.* 2021; 66: 095012. https://doi.org/10.1088/1361-6560/abf51e

OTHER PUBLICATIONS

1. **Ippoliti M**, Makowski M, Schaeffter T, Kolbitsch C. 3D non-rigid motion corrected dynamic contrast enhanced MRI of the liver with high isotropic spatial resolution. In: Proceedings of Joint Annual Meeting ISMRM-ESMRMB, Paris, France; 2018:476.
2. Spincemaille P, Liu Z, Zhang S, **Ippoliti M** et al 2019. Clinical Implementation of Quantitative Susceptibility Mapping: Experience Across Multiple Sites and Scanners. In: Proceedings of Joint Annual Meeting ISMRM-ESMRMB, Paris, France; 2018:5008.
3. **Ippoliti M**, Makowski M, Schaeffter T, Kolbitsch C. 3D non-rigid motion correction for quantitative assessment of hepatic lesions with Dynamic Contrast Enhanced MRI. In: Proceedings of Joint Annual Meeting ISMRM-ESMRMB, Montreal, Canada; 2019:2397.
4. Kolbitsch C, **Ippoliti M**, Makowski M, Brenner W, Schaeffter T. Motion-corrected simultaneous DCE-MRI and PET for hepatic lesion assessment. In: Proceedings of Joint Annual Meeting ISMRM-ESMRMB, Montreal, Canada; 2019:4335.

ACKNOWLEDGEMENT

I would like to thank my supervisors for having supported me throughout my PhD. I would especially like to thank my family and friends for having always supported me throughout my studies. A really special thanks goes to Manuela who not only supported me, but also endured me in my best and worst times. Finally a special thanks goes to my father.